

Dense gas in local galaxies revealed by multiple tracers

Fei Li¹, Junzhi Wang^{1,2*}, Feng Gao³, Shu Liu⁴, Zhi-Yu Zhang⁵, Shanghuo Li^{1,6}
Yan Gong⁷, Juan Li^{1,2} and Yong Shi⁵

¹Shanghai Astronomical Observatory, Chinese Academy of Sciences, 80 Nandan Road, Shanghai, 200030, China

²Key Laboratory of Radio Astronomy, Chinese Academy of Sciences, 10 Yuanhua Road, Nanjing, JiangSu 210033, China

³Max-Planck-Institut für Extraterrestrische Physik, Gießenbachstrasse 1, D-85741 Garching bei München, Germany

⁴CAS Key Laboratory of FAST, National Astronomical Observatories, Chinese Academy of Sciences, Beijing 100012, China

⁵School of Astronomy and Space Science, Nanjing University, Nanjing, 210093, China

⁶Korea Astronomy and Space Science Institute, 776 Daedeokdae-ro, Yuseong-gu, Daejeon 34055, Republic of Korea

⁷Max-Planck-Institut für Radioastronomie, Auf dem Hügel 69, 53121, Bonn, Germany

Accepted XXX. Received YYY; in original form ZZZ

ABSTRACT

We present 3 mm and 2 mm band simultaneously spectroscopic observations of HCN 1-0, HCO⁺ 1-0, HNC 1-0, and CS 3-2 with the IRAM 30 meter telescope, toward a sample of 70 sources as nearby galaxies with infrared luminosities ranging from several 10⁵ L_⊙ to more than 10¹² L_⊙. After combining HCN 1-0, HCO⁺ 1-0 and HNC 1-0 data from literature with our detections, relations between luminosities of dense gas tracers (HCN 1-0, HCO⁺ 1-0 and HNC 1-0) and infrared luminosities are derived, with tight linear correlations for all tracers. Luminosities of CS 3-2 with only our observations also show tight linear correlation with infrared luminosities. No systematic difference is found for tracing dense molecular gas among these tracers. Star formation efficiencies for dense gas with different tracers also do not show any trend along different infrared luminosities. Our study also shows that HCN/HCO⁺ line ratio might not be a good indicator to diagnose obscured AGN in galaxies.

Key words: galaxies: star formation; galaxies: starburst; galaxies: ISM; galaxies: active

1 INTRODUCTION

Dense gas tracers, lines from molecules with high dipole moment (e.g., HCN, HCO⁺, HNC, and CS), which have high critical densities (n_{crit} greater than 10⁴ cm⁻³, directly represent molecular content involved in forming stars (Lada et al. 2012). Observing star-forming molecular gas is one of the direct ways to measure star formation activities in galaxies and in the Milky Way. The star formation law, the relation between star formation rate (SFR) and local gas density, was first proposed by Schmidt (1959) and observationally studied with total gas, including atomic gas traced by HI 21 cm emission and molecular gas traced by CO 1-0 emission, and SFR by Kennicutt (1998). With observations of HCN 1-0 toward 65 galaxies, Gao & Solomon (2004) found a tight linear correlation between the luminosities of HCN 1-0 and infrared emission. This relation has been extended to Galactic dense cores (Wu et al. 2005) and possibly high-z galaxies and QSOs (Gao et al. 2007).

However, since there are several choices of molecules (HCN, HNC, HCO⁺ and CS) with high dipole moments, different masses of dense gas will be obtained with different tracers, with conversion factor of line luminosity to gas mass in galaxies. It was argued if

HCN was a true tracer of dense molecular gas in luminous infrared galaxies (LIRGs) and ultra-luminous infrared galaxies (ULIRGs) (Graciá-Carpio et al. 2006). Further observational results in literature indicated that HCO⁺/HCN 1-0 line ratio varied from 0.36 to 1.83, while HNC/HCN 1-0 ratios were from 0.20 to 1.09 in a sample of 23 galaxies (Costagliola et al. 2011), most of which are (U)LIRGs. Thus, there will be large uncertainties of estimating dense gas masses in individual galaxies with only line luminosity of one dense gas tracer, even though the correlations between line luminosities of different dense gas tracers and IR luminosities have been well established (Gao & Solomon 2004; Wang, Zhang, & Shi 2011; Zhang et al. 2014). Observations of multiple dense gas tracers toward a relatively large sample up to about one hundred of galaxies are essential for determining the uncertainty of estimating dense gas masses there. With these lines detected in galaxies, one can also determine the line ratios between each of them among different types of galaxies: with active galactic nucleus (AGN) or without AGN, starburst or normal star forming galaxies.

The other way for better understanding dense gas properties is to detect optically thin isotopic lines of dense gas tracer with deep observations (Wang et al. 2014, 2016; Li et al. 2020). The isotopic lines of dense gas tracers together with dense gas tracers themselves, can be used to derive optical depths of dense gas tracers, which allows us to constrain dense gas masses more accurately

* E-mail: jzwang@shao.ac.cn

than without isotopic lines. The optical depths of HCN 1-0 derived with HCN/H¹³CN 1-0 line ratios vary from less than 1 to more than 10 in a limited sample of 5 galaxies (Li et al. 2020). Such variation can cause large uncertainty of estimating dense gas masses with line luminosity of HCN 1-0 in galaxies. However, due to the weak intensities of these isotopic lines, only extremely local star forming galaxies or nearby extremely active starburst galaxies with strong line emission can be done for such study. Thus, it is almost impossible to detect isotopic lines of dense gas tracers toward a large sample of galaxies with a reasonable amount of telescope time. Observations of multiple dense gas tracers toward different types of galaxies with infrared luminosities spanning several orders of magnitude will be the best way to testify the consistence of different dense gas tracers in galaxies.

In this paper, we will describe the sample in §2, observation and data reduction in §3, present the main results in §4 and discussions in §5, make the brief summary in §6.

2 THE SAMPLE OF GALAXIES

We obtained new observations for a sample of local galaxies including a wide range of infrared luminosities, from about several $10^5 L_\odot$ to more than $10^{12} L_\odot$ spanning about 7 orders of magnitude. Firstly, 60 sources with bright infrared emission from the IRAS Revised Bright Galaxy Sample (Sanders et al. 2003) with DEC higher than -20° and $F_{100\mu\text{m}} > 30 Jy$ are selected. Sources within that criteria which had been observed by Costagliola et al. (2011) are excluded. Since there are large fraction of sources with L_{IR} between $10^{10} L_\odot$ and $10^{11} L_\odot$, we also excluded some sources within this range, especially if their LST ranges are good for Galactic plane observations. Other ten sources reach this criteria observed with our previous projects are also included. They are six infrared bright galaxies: M 82 (center), NGC 3079, IC 694, Mrk 231, NGC 6240, and NGC 6946 from Li et al. (2020), as well as four different positions along the major axis of M 82 (Li et al. in preparation).

3 OBSERVATIONS AND DATA REDUCTION

3.1 Millimeter spectroscopic observations with IRAM 30m and data reduction

The HCN 1-0, HCO⁺ 1-0, HNC 1-0 and CS 3-2 lines were observed simultaneously with the IRAM 30 meter millimeter telescope (IRAM 30m) at Pico Veleta, Spain on February, May, July and August 2019. The critical densities of HCN 1-0, HCO⁺ 1-0, HNC 1-0 and CS 3-2 are $6.8 \times 10^4 \text{cm}^{-3}$, $4.7 \times 10^5 \text{cm}^{-3}$, $1.4 \times 10^5 \text{cm}^{-3}$, and $4.4 \times 10^5 \text{cm}^{-3}$, when kinematic temperature of H₂ is 10 K, while the effective excitation densities for these lines are about 1/50 of the critical densities (Shirley 2015).

We used the 3 mm (E0) and 2mm (E1) band of The Eight Mixer Receiver (EMIR) simultaneously and the Fourier Transform Spectrometers (FTS) backend to cover 8 GHz bandwidth and 195 kHz spectral resolution for each band with dual polarization. Standard wobbler switching mode with beam throws of $\pm 60''$ and a switching frequency of 0.5 Hz were used. The beam sizes of IRAM 30m range from FWHM $\sim 28''$ at 88 GHz to $\sim 17''$ at 146 GHz. The typical system temperatures are around 100 K in the 3-mm band and around 150 K in the 2-mm band. The detailed informations of the sample are shown in Table 1, which includes source name, coordinates, IRAS 100 μm flux, cz and luminosity distance (Sanders et al. 2003), as well as observing dates, telescope time (ON+OFF)

and typical system temperature at 3mm band. Observations done in 2017 and 2019 Feb are with project 058-17 (Li et al. 2020) and 186-18 (Li et al. in preparation), respectively, while the rest observations are all with project 066-19. The weather varies from good ($p_{wv} \sim 3.8 \text{ mm}$) to mediocre ($p_{wv} \sim 9.4 \text{ mm}$) conditions during the observations. Pointing was checked every 2 h with nearby strong millimetre emitting quasi-stellar objects. We also checked and corrected the focus at the beginning of each run and during sunsets and sunrises. The antenna temperature (T_A^*) was converted to the main beam brightness temperature (T_{mb}), using $T_{\text{mb}} = T_A^* \cdot F_{\text{eff}} / B_{\text{eff}}$, where the forward efficiency F_{eff} is 0.95 and beam efficiency B_{eff} is 0.81 for 3 mm band, while F_{eff} is 0.93 and B_{eff} is 0.73 for 2 mm band. Each scan consists of 2 minutes with an on-source integration of 1 minute. The total telescope time (ON+OFF) was about one hour towards each source.

Data reduction was conducted with the class package, which is a part of the GILDAS¹ software. Firstly, each individual spectrum was checked. Then, we discarded the spectra with issues related to their baseline flatness, standing wave, system temperature, etc. Most of the spectra have good qualities. All reliable spectra of a given source tuned at the same frequency were averaged into one spectrum. A first-order polynomial baseline was fitted and subtracted from the averaged spectrum. Due to the broad line widths of these galaxies, the final spectra were smoothed to a velocity spacing of $\sim 20\text{--}40 \text{ km s}^{-1}$. The rest frequencies of each line from the NIST database² were used for the line identification.

3.2 Infrared data and line luminosities

To measure the total infrared luminosities L_{IR} ($3 \mu\text{m} - 1000 \mu\text{m}$), we obtained infrared archival imaging data from *Spitzer* MIPS and *Herschel* PACS instruments from the NASA/IPAC Infrared Science Archive (IRSA). The data have been processed to level 2 for MIPS 24 μm and level 2.5 or 3 for PACS 70 μm , 100 μm , and 160 μm bands. To match the molecular emission, the infrared luminosities have been corrected from the whole galaxy to the region within the IRAM 30-m telescope beam. Following the same approach as adopted by Tan et al. (2018), *Spitzer* and *Herschel* data have been convolved to $28''$ and $17''$ resolution, corresponding to the beam-size of the 3 mm and 2 mm band, respectively. For the galaxies with only *Spitzer* MIPS 24 μm image, we used MIPS 24 μm image to obtain the ratio of such a region to the whole galaxy. Then, with the 24 μm flux ratio, we estimated the infrared luminosity within the beam by scaling the total infrared luminosity from Sanders et al. (2003), which is similar to the method in Wang, Zhang, & Shi (2011). We computed the line luminosities for all dense gas tracers using equation (2) in Gao & Solomon (2004) for all galaxies:

$$L'_{\text{gas}} \approx \pi / (4 \ln 2) \theta^2 I_{\text{HCN}} d_L^2 (1+z)^{-3} [\text{K km s}^{-1} \text{ pc}^2] \quad (1)$$

where I_{HCN} is the observed integrated line intensity, d_L^2 is the luminosity distance.

The infrared luminosity is calculated from

$$L_{\text{TIR}} = \sum c_i \nu L_\nu(i) L_\odot \quad (2)$$

where c_i is the calibration coefficients for various combinations of bands, $\nu L_\nu(i)$ is the resolved luminosity in a given band i in units

¹ <http://www.iram.fr/IRAMFR/GILDAS>

² <https://pml.nist.gov/cgi-bin/micro/table5/start.pl>

of L_{\odot} (Tan et al. 2018). The values of c_i are from Tan et al. (2018). The total error estimated for L_{TIR} includes errors of photometry of $\sim 5\%$ (Balog et al. 2014), the flux calibration error of $\sim 5\%$, and the error of tracing TIR with a combined IR band of $\sim 20\%$ (Galametz et al. 2013).

4 RESULTS

4.1 Detections of dense gas tracers in local galaxies with IRAM 30 meter

The targets with new observations, which include 70 sources, are listed in Table 1. Dense gas tracers in these sources were detected with detection rate of 89%, 90%, 73%, and 51% for HCN 1-0, HCO⁺ 1-0, HNC 1-0 and CS 3-2, respectively. The velocity-integrated intensities of these four lines are shown in Table 2. For HCN 1-0 and HCO⁺ 1-0, most of them are solid detections above 5σ , while, some marginal detections at $\sim 3\sigma$ to 4σ level are shown for HNC 1-0 and CS 3-2. 3σ upper limits for the velocity-integrated intensity of the undetected lines are also derived. The 3σ upper limits are calculated from $\sigma_{\text{line}} = \text{RMS}_{\text{channel}} \sqrt{\Delta\mu \times \delta V}$, where $\text{RMS}_{\text{channel}}$ is the baseline rms of the smoothed spectrum at ~ 30 km/s–40 km/s and $\Delta\mu$ is the line width and δV is the channel width. For the sources of non-detection in all four species, including NGC 2403, NGC 4605, NGC 4654 and NGC 6822, we use the CO line width to estimate the upper limits of velocity-integrated intensity, due to the central velocity of HCN 1-0 is consistent with that of the detected lines of CO 1-0 (Israel, Tacconi, & Baas 1995) and CO 3-2 (Mao et al. 2010). For the other sources, we use line width of the detected lines to estimate the upper limits of velocity-integrated intensity of the undetected lines for the same source. Note that CS 3-2 is not covered by the observed frequency range in Mrk 231 and NGC 6240. The spectra of these dense gas tracers are shown in Figure A1, with the grey shaded region in each subfigure to indicate velocity range of identified detections.

For comparison, Arp 220, which was included in Privon et al. (2015), is also observed. However, fluxes measured by our observations are only about 70% of that in Privon et al. (2015). Our fluxes are consistent with results reported in Greve et al. (2009) and Wang et al. (2016). We speculate the mis-match of line fluxes of Arp 220 in Privon et al. (2015) may be due to poor velocity resolution, which can cause un-resolved absorption dip at central velocity (Greve et al. 2009; Wang et al. 2016), or poor baselines, which can cause over-estimation of line widths. Another evidence that such different fluxes can not be caused by the pointing error of our observation is that the peak emissions are similar in all observations (Greve et al. 2009; Privon et al. 2015; Wang et al. 2016), which is about 17mK (T_{mb}) for HCN 1-0 (see Figure A1). Since line widths in most of other sources in Privon et al. (2015) are not as broad as that in Arp 220 and absorption dip is not as important as that in Arp 220, such mis-match of line fluxes in Privon et al. (2015) should not be a big issue.

Mrk 231, NGC 3079, NGC 4194, NGC 4418 and NGC 6240 were also included both in Costagliola et al. (2011) and our observations, with similar velocity integrated fluxes. Results from our observations are used in discussion. By combining our new IRAM data with literature data, including 57 local (U)LIRGs (Privon et al. 2015) and 12 local galaxies (Costagliola et al. 2011), we reconstruct a sample of 140 galaxies with HCN 1-0, HCO⁺ 1-0 and HNC 1-0 observations, containing 125, 124, 85 detections, respectively.

4.2 The luminosities of dense gas tracers v.s. infrared luminosities

The correlations between L_{IR} and $L'_{\text{dense gas}}$ (HCN 1-0, HCO⁺ 1-0, and HNC 1-0, and CS 3-2) are presented in Figure 1, with the data listed in Table 3, including our data with new observations as well as HCN 1-0, HCO⁺ 1-0 and HNC 1-0 detections in local galaxies from literature (Costagliola et al. 2011; Privon et al. 2015). We adopt the Markov Chain Monte Carlo (MCMC) method using package emcee (Foreman-Mackey et al. 2013) to account for measurement uncertainties. Only detections are adopted to fit the relationship, while the upper limits are just plotted in the Figures. The L_{IR} of sample galaxies span 7 orders of magnitude from a few $10^5 L_{\odot}$ to several times of $10^{12} L_{\odot}$. However, dense gas tracers are not detected in the low infrared luminosity galaxies, including NGC 6822, NGC 2403, and NGC 4605. Thus, the lowest infrared luminosity with detection of dense gas tracers (HCN and HCO⁺ 1-0) is NGC 4605 with $\log(L_{\text{IR}}) = 7.82$, while it is $\log(L_{\text{IR}}) = 7.5$ in NGC 2976 with CS 3-2 detection. Note that due to different beam sizes, there are large difference of $\log(L_{\text{IR}})$ for regions corresponding to HCN 1-0 and CS 3-2 (see Table 3), such as that in NGC 2976. The overall spanning of L_{IR} is about 5 orders of magnitude with detections of dense gas tracers. In the following, the fitted slope and uncertainties are the median and one standard deviation of the resulting MCMC chain:

$$\text{Log}(L_{\text{IR}}) = 0.97(\pm 0.01)\text{Log}(L_{\text{HCN}}) + 3.35(\pm 0.09) \quad (3)$$

$$\text{Log}(L_{\text{IR}}) = 0.95(\pm 0.01)\text{Log}(L_{\text{HCO}^+}) + 3.59(\pm 0.09) \quad (4)$$

$$\text{Log}(L_{\text{IR}}) = 0.97(\pm 0.02)\text{Log}(L_{\text{HNC}}) + 3.75(\pm 0.11) \quad (5)$$

$$\text{Log}(L_{\text{IR}}) = 1.07(\pm 0.03)\text{Log}(L_{\text{CS}}) + 2.95(\pm 0.19) \quad (6)$$

The fitting results are shown as the black solid line in Figure 1, with a Spearman rank correlation coefficient of 0.91, 0.94, 0.91 and 0.83, for HCN 1-0, HCO⁺ 1-0, HNC 1-0, and CS 3-2, respectively. As shown with blue dotted line in this figure, only our IRAM data were used to fit the relationship, which gave a similar slope of 1.03 ± 0.02 , 0.99 ± 0.02 and 1.01 ± 0.02 for HCN 1-0, HCO⁺ 1-0 and HNC 1-0, yielding a Spearman rank correlation coefficient (r_s) of 0.83, 0.85 and 0.86, respectively, with worse Spearman rank correlation coefficient than the whole sample, which should mainly due to less sources in only our data than the whole sample. On the other hand, no clear difference of correlation coefficient, can be found among the four tracers, which is from a Spearman rank correlation analysis.

5 DISCUSSION

5.1 Dense gas star formation law derived with different dense gas tracers

Dense molecular gas and star formation had been studied from the relation between HCN 1-0 and infrared luminosities (Solomon, Downes, & Radford 1992; Gao & Solomon 2004), with a tight linear correlation. However, unlike low- J CO lines as total molecular gas tracers, there are many choices of dense gas tracers with transitions of high dipole moment molecules, such as HCN, HCO⁺, HNC, CS,

CN, and HC_3N . Even though there are dense gas tracers other than HCN 1-0 which also provide linear correlation in the past years: CS 5-4 (Wang, Zhang, & Shi 2011), HCN 4-3, CS 7-6 and HCO^+ 4-3 (Zhang et al. 2014), and HCN 3-2 (Li et al. 2020), sub-linear relation with slope of 0.79 ± 0.09 for HCN 3-2 (Bussmann et al. 2008) and super-linear relation with HCN 1-0 (Graciá-Carpio et al. 2008; García-Burillo et al. 2012) were also reported. However, the sub-linear slope of L_{IR} and $L'_{\text{HCN}_{3-2}}$ reported in Bussmann et al. (2008) is mainly caused by over-estimation of L_{IR} in galaxies with HCN 3-2 emission, because the beam size of SMT for HCN 3-2 observations is smaller than the sizes of nearby galaxies. After correcting the infrared emission to the same as observed HCN 3-2, a linear correlation was derived (Li et al. 2020). On the other hand, far-IR luminosities instead of IR luminosities are used in Graciá-Carpio et al. (2008) and García-Burillo et al. (2012), which may be the main reason of super linear correlation since linear correlation was obtained with a similar sample by Privon et al. (2015).

As shown in Figure 1, the relations between the line luminosities of HCN 1-0, HCO^+ 1-0, HNC 1-0, and CS 3-2 and infrared luminosity are all close to linear correlation. All the data, including our observations and that from Privon et al. (2015) and Costagliola et al. (2011), used in Figure 1, are observed with IRAM 30m, which provides the same beam size for each line to avoid the problem of beam matching for different observations. The high Spearman rank correlation coefficients between infrared luminosities and luminosities of HCN 1-0, HCO^+ 1-0, HNC 1-0 and CS 3-2 with slopes close to unity indicate that even though there might be several times uncertainties of the conversion factor from line luminosity of dense gas tracers to dense molecular gas mass in individual galaxy, no clear systematic bias of such conversion factor for different tracers. The star formation law obtained with different dense gas tracers is consistent with each other. Note that not only the detections follow the good correlation in Figure 1, but also the upper limits agree well with the relation, with infrared luminosities spanning 7 orders of magnitude. However, since the normally used dense gas tracers are optically thick, the self absorption of these lines, as well as the abundance issue due to different chemical conditions, such as radiation field and shocks, can cause large uncertainties of estimating dense gas mass from only one line. Such uncertainties may be the main reason of the scatter in the relation plotted in Figure 1.

5.2 Possible reason for sources with deviation from the correlation and note for several individual sources

Even though the relations between luminosities of dense gas tracers and infrared luminosities are pretty tight with high Spearman rank correlation coefficients for HCN 1-0, HCO^+ 1-0, HNC 1-0, and CS 3-2, there are large scatters up to about 10 times for some sources (see Figure 1). Such deviation may be real for those sources because of low or high star formation efficiency for dense gas, or the uncertainties of converting dense gas mass from line luminosity of dense gas tracers, since the observational parameters are only line fluxes, which can be used to obtain line luminosities with known distances. For the conversion factor from line luminosity to dense gas mass, several properties can cause the uncertainty, including optical depth, excitation conditions (density and temperature), and abundance of dense gas tracers caused by metallicity and other properties such as PDRs. However, since star formation rates, traced by infrared luminosities or hydrogen recombination lines, such as $\text{H}\alpha$, is counting for massive young stars, while dense gas traced by those dense gas tracers is counting for the gas that will form stars in the near future, the correlation can break if there are large differences

of star formation evolutions in different galaxies. Another effect that can overestimate star formation rate from infrared luminosity is AGN contribution, especially in galaxies with low star formation activities.

There are several sources, which are not detected in one or more lines, should be noted for deviation from the correlation in Figure 1. No detections were found for all four lines in NGC 2403, NGC 4605 and NGC 6822. Even though they are in the regions away from the fitting lines, they are still consistent with the correlation, since they are upper limits of line emission. If the lines can be detected with more sensitive observations, it should be closer to the fitted lines or even at the other side of the lines. Based on the current results, the real deviations can be seen for NGC 4527, NGC 4536, NGC 3810, and NGC 5907. Especially, only HCO^+ 1-0 is detected in NGC 4536 at 4.5σ level, while other three lines remain non-detected. If the conversion factor of dense gas mass from dense gas tracer luminosity in these sources are similar to that of other galaxies, it will imply that there are less dense gas than expected. In NGC 4536, the metallicity is within normal range and with strong CO 1-0 ($525.67 \pm 4.49 \text{ Jy km s}^{-1}$) and ^{13}CO 1-0 ($54.51 \pm 3.98 \text{ Jy km s}^{-1}$) emission (Cao et al. 2017). While even HCO^+ 1-0 detected in NGC 4536 is only $0.23 \pm 0.05 \text{ K km s}^{-1}$, which corresponds to about 1.2 Jy km s^{-1} . The dense gas fraction is really low, based on the line ratio of HCN and HCO^+ 1-0 to CO and ^{13}CO 1-0. For comparison, the line ratio of CO/HCN 1-0 in starburst galaxies are normally around 10 (Aalto et al. 2002), much lower than in NGC 4536. No AGN activity is found in NGC 4536. Thus, we suggest that the most possible reason for the lack of dense gas in these galaxies, including NGC 4536, is that star formation activities are at late evolutionary stages with strong feedback to the molecular gas, which causes the low dense gas fraction.

5.3 Star formation efficiency v.s. infrared luminosity revealed by different dense gas tracers

Star formation efficiency (SFE) of dense gas, $\text{SFR}/M_{\text{dense}}$, can be derived with $L_{\text{IR}}/L_{\text{dense}}$. With $L_{\text{FIR}}/L_{\text{HCN}}$ ratio for galaxies with L_{FIR} between $10^{10}L_{\odot}$ to several times of $10^{13}L_{\odot}$, García-Burillo et al. (2012) claimed that SFE increased with the increment of SFR (L_{FIR}), with large scatter. However, no clear trends of $L'_{\text{HCN}}/L_{\text{IR}}$ and L_{IR} , or $L_{\text{HCO}^+}/L_{\text{IR}}$ and L_{IR} were found in Privon et al. (2015).

Figure 2 shows the $L'_{\text{dense}}/L_{\text{IR}}$ versus L_{IR} , including our new data and literature data from Privon et al. (2015) and Costagliola et al. (2011). No trend of $L'_{\text{dense}}/L_{\text{IR}}$ versus L_{IR} can be found for HCN 1-0, HCO^+ 1-0, and HNC 1-0, with L_{IR} spanning range larger than that discussed in García-Burillo et al. (2012) and Privon et al. (2015). On the other hand, $L'_{\text{dense}}/L_{\text{IR}}$ can vary more than ten times for different galaxies with similar L_{IR} . In figures 2, 3, and 4, the sources marked as ‘‘AGN’’ are identified with AGN activity from NED³, while sources marked as ‘‘No AGN’’ are without known AGN activity also from NED. However, some of ‘‘No AGN’’ sources may still be with AGN activity.

Sources with known AGN activities do not show clear difference when compared with those without known AGN activities. Thus, the dense gas depletion time to form stars from dense molecular gas, does not relate to SFR traced by infrared luminosity. No bias can be found for different dense gas tracers (HCN 1-0, HCO^+

³ The NASA/IPAC Extragalactic Database (NED) is funded by the National Aeronautics and Space Administration and operated by the California Institute of Technology.

1-0 and HNC 1-0), or with or without known AGN activities. We would like to suggest that star formation from dense molecular gas follows the similar law in different galaxies: low or high SFR, with or without known AGN. However, the dense gas fraction: the ratio of dense gas to total molecular gas, and molecular gas to atomic gas ratio, which are important to affect star formation from gas, still need to be studied for understanding star formation efficiency in different types of galaxies. Metallicities, merging history, AGN feedback, and other properties, can affect star formation in galaxies. The formation from atomic gas to molecular gas, the collapse of molecular clouds to dense cores, should be understood in further studies, which may also be compared with gas to star ratios in different galaxies.

5.4 Line ratios between different dense gas tracers in individual galaxies

HCN/HCO⁺ line ratio had been used to distinguish between AGNs and starburst signatures in galactic centers (Kohno et al. 2001; Imanishi et al. 2004, 2007; Krips et al. 2008), while HCN/HNC ratio together with HCN/CN ratio had been used to discuss starburst evolution in galaxies (Aalto et al. 2002). With HCN/HCO⁺ 4-3 ratio and CS 7-6 ratio in a sample of galaxies with AGN or without known AGN, Izumi et al. (2013, 2016) and Krips et al. (2008) suggested that HCN can be enhanced in AGNs and HCN/HCO⁺ line ratio can be used to diagnose AGN and starburst contribution in galaxies. Lower average HCN/HCO⁺ 1-0 line ratio in LIRGS and starbursts than that in AGNs was found in a limited sample (Costagliola et al. 2011), which was consistent with the weak trend found in Kohno et al. (2001) and Imanishi et al. (2007).

However, with limited sample of galaxies in Krips et al. (2008), Costagliola et al. (2011) and Izumi et al. (2013, 2016), it is hard to conclude if such line ratios can be used to diagnose AGN and/or starburst in galaxies, since some exceptions of HCN/HCO⁺ line ratio had been found in literature: a sample of (U)LIRGs (Privon et al. 2015), and NGC 4258 with AGN (Li et al. 2019). With the sample including our observations and that from Costagliola et al. (2011) and Privon et al. (2015), we compiled a sample with more than 100 galaxies, with detection of a least two lines of HCN, HCO⁺, and HNC 1-0. The plots of line ratios of HCN/HCO⁺ 1-0 and HCN/HNC 1-0 versus infrared luminosities and luminosity distances are presented in Figure 3. HCN/HCO⁺ 1-0 ratio varies from about 0.38 in IC 1623 (Privon et al. 2015) to 2.2 in NGC 4535 (see Table 2), while HCN/HNC 1-0 ratio varies from 0.86 in NGC 891 to 4.3 in NGC 2903 (see Table 2). No clear trend was found for the line ratios and infrared luminosities, which is consistent with the results for HCN/HCO⁺ 1-0 ratio in Privon et al. (2015). With HCN and HCO⁺ 1-0 data in a large sample of galaxies observed simultaneously in Costagliola et al. (2011), Privon et al. (2015) and our observations, which can avoid errors of flux ratio due to the uncertainties of absolute flux calibration and pointing errors with different observations, HCN/HCO⁺ 1-0 ratios in these galaxies do not vary with different infrared luminosities, however, with large scatters even with similar infrared luminosities (see Figure 3). Thus, different HCN/HCO⁺ 1-0 ratios in galaxies should not be caused by star formation activities, as suggested by Graciá-Carpio et al. (2006) for higher HCN/HCO⁺ ratios in ULIRGs than galaxies with lower infrared luminosity.

Red dashed lines represent averaged values with x -axis bins for “AGN” sources, while black lines for “No AGN” sources, are also presented in Figure 3. No clear difference between these two sub-groups: “AGN” and “No AGN”, is found in Figure 3. Abundance,

opacity and excitation of HCN and HCO⁺ molecules can affect the line ratio of HCN/HCO⁺ 1-0. Even if starburst activities, which cause strong photon dominated regions (PDRs), or AGN activities, which cause strong X-ray dominated regions (XDRs), may enhance HCN or HCO⁺ abundances, it is hard to use line ratio of such optically thick lines: HCN and HCO⁺ 1-0, to derive the abundance ratio of HCN and HCO⁺. Such line ratio may not be a good tracer of AGN activity had been pointed out by Costagliola et al. (2011) and Privon et al. (2015) with smaller sample than ours. With the comparison with X-ray emission, Privon et al. (2020) had pointed out that HCN/HCO⁺ line ratios can not be a reliable method to find AGN, which is consistent with our results.

As optically thin lines, H¹³CN and H¹³CO⁺ 1-0, the isotopic lines of HCN and HCO⁺, will be a better choice than HCN and HCO⁺ 1-0 to derive abundance ratio of HCN and HCO⁺. However, it is hard to do large sample survey due to weak emission of these isotopic lines, which are normally several times to tens of times weaker than their main isotopic lines, as seen in NGC 1068 (Wang et al. 2014), Arp 220 (Wang et al. 2016), Mrk 231 (Lindberg et al. 2016; Li et al. 2020), M82 and NGC 3079 (Li et al. 2020), and NGC 4418 (Costagliola et al. 2015; Li et al. 2020). ALMA observations of H¹³CN and H¹³CO⁺ lines toward local galaxies in the future will help us to determine the enhancement of these molecules due to starburst or AGN activities.

Neither any trend of HCN/HNC 1-0 ratio along with infrared luminosity, nor clear difference between “AGN” and “No AGN” groups for HCN/HNC 1-0 ratios versus infrared luminosities, can be found (see Figure 3). We also notice that the sources with low HCN/HNC 1-0 ratios in Aalto et al. (2002): 1.0 in IC 694 and Mrk 231 may not be real. With better sensitivity than that in Aalto et al. (2002) and simultaneous observation, our data show that this ratio is 3.6 ± 0.4 in IC 694 and 2.3 ± 0.1 in Mrk 231 (see Table 2). Especially, the simultaneous observation can avoid the uncertainties of pointing error to obtain the line ratio. Similar to that of determining possible enhancement of HCN or HCO⁺ molecules due to starburst or AGN activities, optically thin isotopic lines of HCN and HNC 1-0 should be used to derive HCN/HNC abundance ratio, even if this ratio can reflect starburst evolution with gas phase chemistry in molecular clouds.

HCN/HCO⁺ 1-0 and HCN/HNC 1-0 ratios versus luminosity distances are also presented in Figure 3. Since the beam of IRAM 30m at 3mm band can cover only central region of nearby galaxies, while it can cover entire galaxy for distant sources. There is no obvious trend of HCN/HCO⁺ 1-0 and HCN/HNC 1-0 ratios with distance (see Figure 3). Thus, the covering area of one galaxy with IRAM 30m beam ($\sim 28''$) is not a dominate factor for the line ratios, which is consistent with that in Privon et al. (2015).

We also try to use the combination of HCN/HCO⁺ 1-0 and HCN/HNC 1-0 ratio to determine the effect of AGN and starburst activities. Plots of HCN/HCO⁺ 1-0 and HCN/HNC 1-0 ratios are presented in Figure 4. In the left of Figure 4, the sample is separated into two sub-groups as “AGN” in red and “No AGN” in blue, while it is separated into two sub-groups with $L_{\text{IR}} > 10^{10} L_{\odot}$ in blue and $L_{\text{IR}} < 10^{10} L_{\odot}$ in red at the right of Figure 4. It is impossible to separate “AGN” and “No AGN”, or starburst and normal star forming galaxies, with the combination of HCN/HCO⁺ 1-0 and HCN/HNC 1-0 ratios.

6 SUMMARY AND CONCLUSION REMARKS

With simultaneous observations of HCN 1-0, HCO⁺ 1-0, HNC 1-0, and CS 3-2 toward 70 local galaxies with a wide infrared luminosity coverage from several $10^5 L_{\odot}$ to more than $10^{12} L_{\odot}$, we detected these lines with detection rate of 89%, 90%, 73%, and 51%, respectively. After combining data from literature (Privon et al. 2015; Costagliola et al. 2011), we compiled a sample of 140 galaxies with simultaneous observations of HCN 1-0, HCO⁺ 1-0, and HNC 1-0. With comparison of luminosities of dense gas tracers and infrared luminosity, line ratios, the main conclusions are listed below:

1. The slopes of global relations between luminosities of dense gas tracers (HCN 1-0, HCO⁺ 1-0, HNC 1-0, and CS 3-2) and infrared luminosities are close to unity. Even though there may be several times uncertainties of estimating dense gas mass in individual galaxy from one dense gas tracer, these dense gas tracers give similar results for dense gas star formation law.

2. No clear trend is found for the relation between infrared luminosities and star formation efficiencies derived with HCN 1-0, HCO⁺ 1-0 and HNC 1-0, which means that dense gas depletion time to form stars from dense molecular gas does not relate to SFR.

3. HCN/HCO⁺ line ratio can not be a good tool to diagnose obscured AGN in galaxies. Even combining with HCN/HNC line ratio will not improve such diagnostic.

ACKNOWLEDGEMENTS

This work is supported by the National Natural Science Foundation of China grant 11590783, and U1731237. This study is based on observations carried out under project number 066-19, 186-18 and 058-17 with the IRAM 30-m telescope. IRAM is supported by INSU/CNRS (France), MPG (Germany) and IGN (Spain). This research has made use of the NASA/IPAC Extragalactic Database, which is funded by the National Aeronautics and Space Administration and operated by the California Institute of Technology.

DATA AVAILABILITY

The original data observed with IRAM 30 meter can be accessed by IRAM archive system at <https://www.iram-institute.org/EN/content-page-386-7-386-0-0-0.html>. If anyone is interested in the reduced data presented in this paper, please contact Junzhi Wang at jzwang@shao.ac.cn.

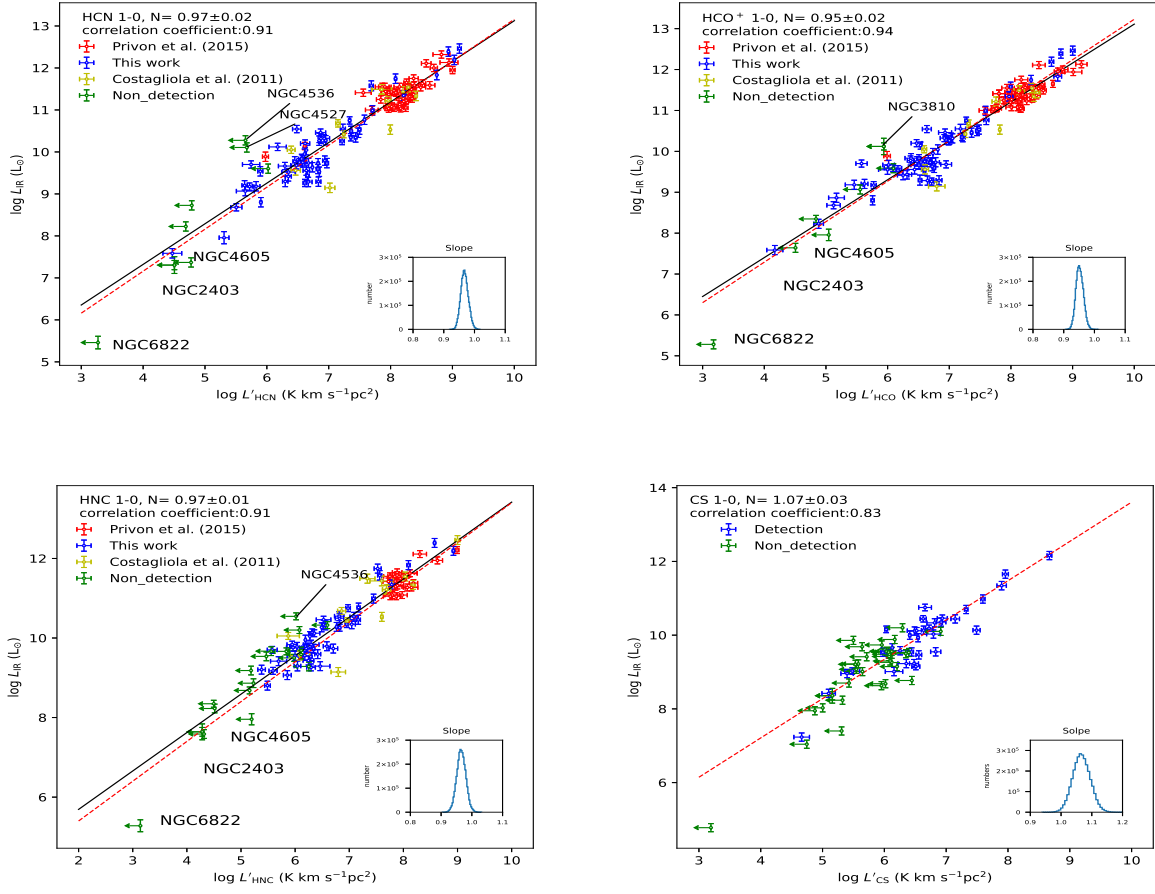


Figure 1. The relations between the gas luminosity $\log(L'_{\text{dense gas}})$ and the IR luminosity $\log(L_{\text{IR}})$. The circles are the sources with detected dense gas tracers from our data in blue, and literature in red (Privon et al. 2015) and yellow (Costagliola et al. 2011), respectively. The points in green are sources with non-detected dense gas tracers from our data and the literature data. The upper limits are not adopted in the fitting. The inset panels show the probability density distribution of the slopes derived from the Bayesian fitting. Upper left: HCN 1-0, Upper right: HCO⁺ 1-0, Lower left: HNC 1-0, Lower right: CS 3-2. In these four panels, the red solid lines indicate the best-fit relations of Equations (4)-(6) respectively, using the all data. While, the blue dotted lines show the relation using our IRAM data alone.

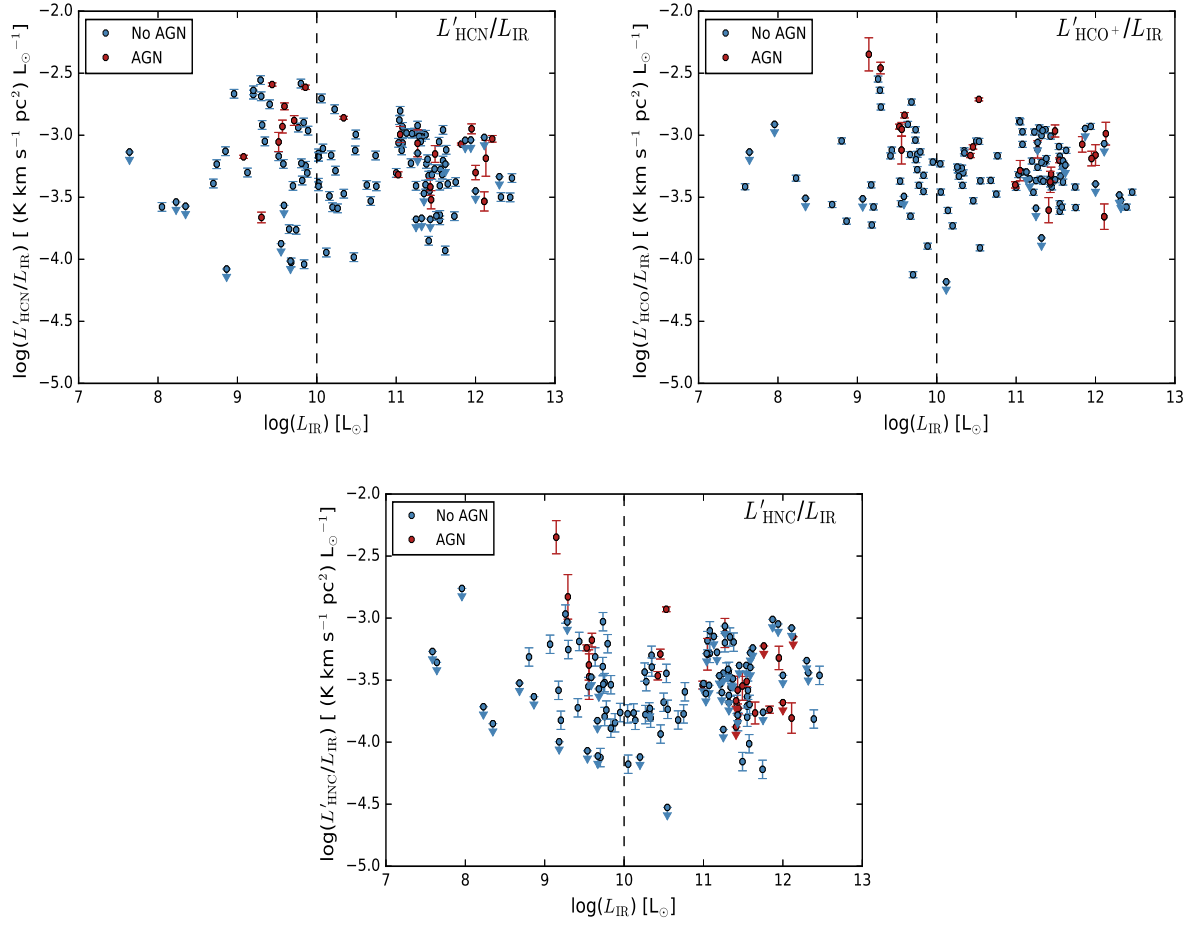


Figure 2. The relation between star formation efficiency derived with different dense gas tracers and infrared luminosities. Upper left: $L'_{\text{HCN}}/L_{\text{IR}}$ vs. L_{IR} . Upper right: $L'_{\text{HCO}^+}/L_{\text{IR}}$ vs. L_{IR} . Lower: $L'_{\text{HNC}}/L_{\text{IR}}$ vs. L_{IR} . These sources are from Table 3. The sources marked as “AGN” are identified with AGN activity from literature, while sources marked as “No AGN” are without known AGN activity in the literature. However, some of “No AGN” sources may still be with AGN activity.

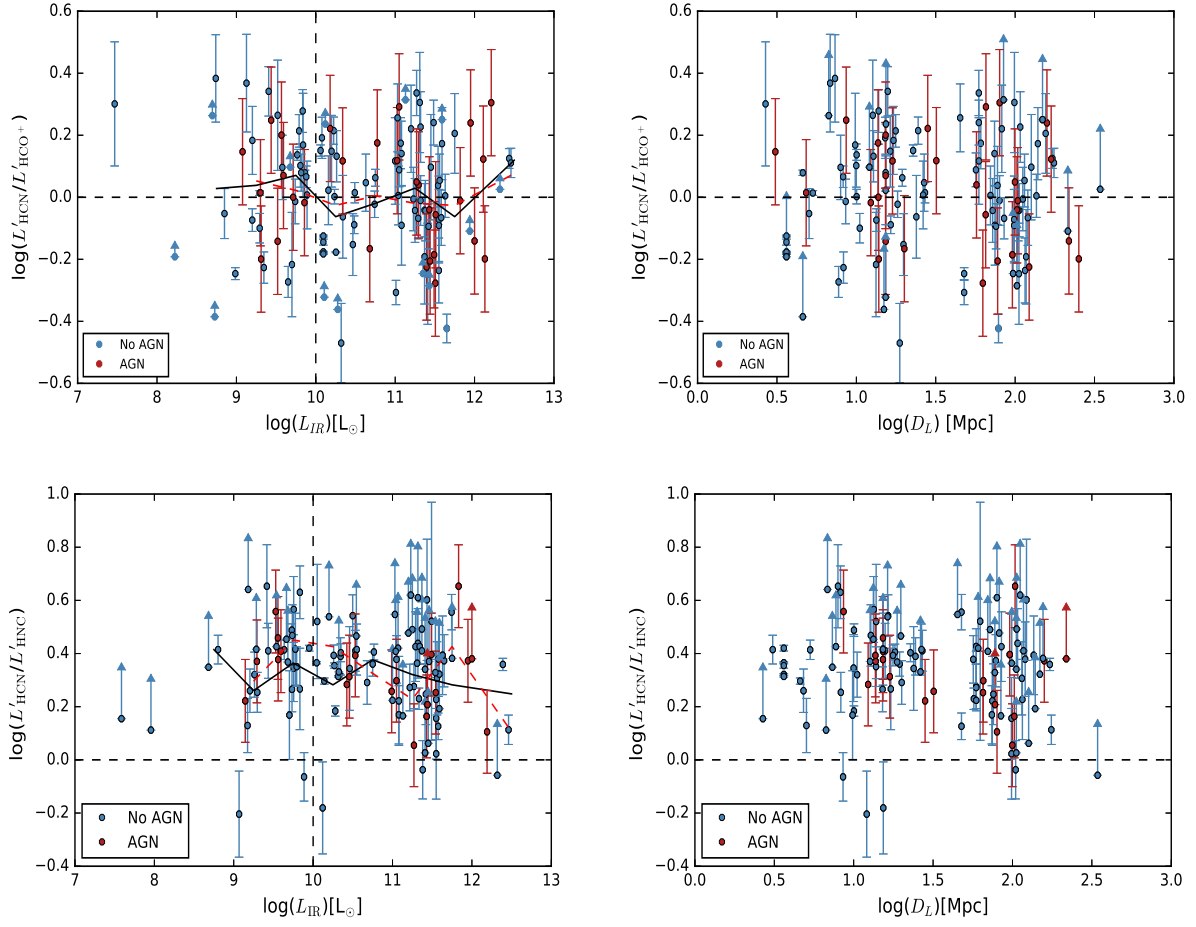


Figure 3. HCN/HCO⁺ 1-0 line ratios as a function of IR luminosity (upper left) and luminosity distance (upper right), as well as HCN/HNC 1-0 ratio as a function of IR luminosity (lower left) and luminosity distance (lower right). In these four panels, the black solid lines indicate mean luminosity ratios of dense gas tracers for the sources without known AGN activity. While, the red dotted lines show the result from the source with AGN activity. The black dotted lines imply that ratios equal one.

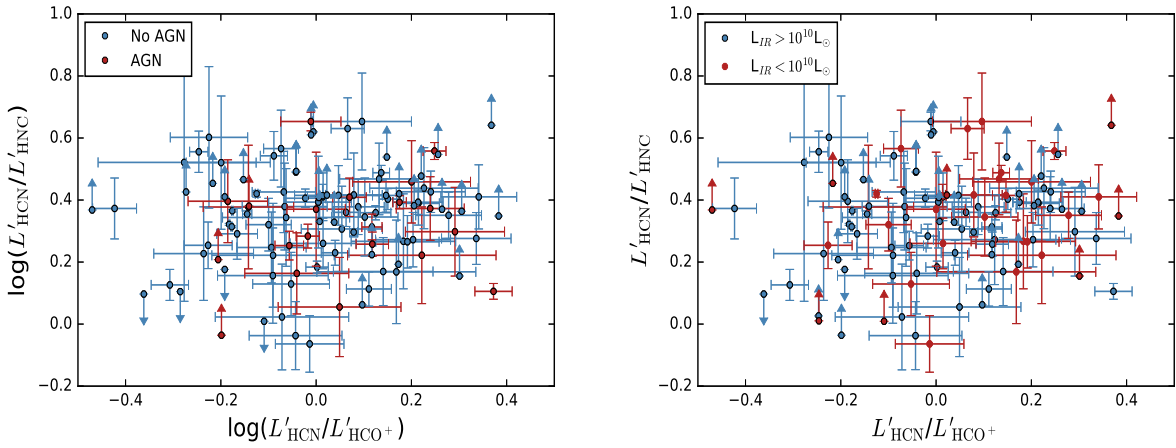


Figure 4. HCN/HCO⁺ 1-0 ratios and HCN/HNC 1-0 ratios in this sample. Left: “AGN” with red points and “No AGN” with blue points. Right: red points for sources with infrared luminosities less than $10^{10}L_{\odot}$ and blue points for infrared luminosities greater than $10^{10}L_{\odot}$.

Table 1: Galaxies Observed with IRAM 30-m Telescope

Source Name	RA (J2000)	DEC (J2000)	$F_{100\mu m}$ (Jy)	cz km s^{-1}	Distance (Mpc)	Obs Month (YYYY MM)	t_{int} (minutes)	T_{sys} (K)
NGC 891	02:22:33.5	+42:21:18	172.23	533	8.57	2019 Aug	80	103
IC 342	03:46:49.4	+68:05:49	391.66	31	4.60	2019 Aug	20	100
UGC 02855	03:48:19.4	+70:08:03	89.18	1184	19.46	2019 Aug	100	108
NGC 1569	04:30:49.5	+64:51:01	55.29	-97	4.60	2019 Aug	102	126
NGC 2146	06:18:39.8	+78:21:25	194.05	885	16.47	2019 Aug	61	122
NGC 2403	07:36:51.3	+65:36:30	99.13	161	3.22	2019 Aug	81	101
NGC 2683	08:52:40.1	+33:25:23	30.68	425	7.34	2019 Aug	204	122
NGC 2903	09:32:10.5	+21:30:05	130.43	566	8.26	2019 Jul	37	99
NGC 2976	09:47:14.5	+67:55:10	33.43	11	2.68	2019 Aug	86	106
NGC 3031	09:55:33.6	+69:03:56	174.02	-34	3.63	2019 Aug	88	107
M82_1	09:55:48.0	+69:40:40	1373.69	187	3.63	2019 Feb	115	83
M82_2	09:55:50.0	+69:40:43	1373.69	187	3.63	2019 Feb	116	94
M82_3(center)	09:55:53.1	+69:40:41	1373.69	187	3.63	2017 Jul	106	145
M82_4	09:55:55.0	+69:40:50	1373.69	187	3.63	2019 Feb	118	134
M82_5	09:55:57.0	+69:40:55	1373.69	187	3.63	2019 Feb	89	101
NGC 3079	10:01:57.9	+55:40:51	104.69	1166	16.1	2017 Jul	122	90
NGC 3310	10:38:46.2	+53:30:08	44.19	1060	19.81	2019 Feb	120	83
NGC 3351	10:43:58.1	+11:42:10	41.10	769	9.99	2019 Jul	65	112
NGC 3368	10:46:45.6	+11:49:13	31.63	916	10.51	2019 Jul	47	93
NGC 3504	11:03:11.1	+27:58:22	34.05	1550	27.07	2017 Jul	67	99
NGC 3521	11:05:49.2	-00:02:15.0	121.76	736	6.84	2019 Feb	102	90
NGC 3593	11:14:37.4	+12:49:02	36.44	578	5.04	2019 Jul	64	91
NGC 3627	11:20:15.3	+12:59:32	136.56	740	10.04	2019 Feb	85	87
NGC 3628	11:20:17.4	+13:35:19	105.76	825	10.04	2019 Feb	52	90
NGC 3675	11:26:09.0	+43:35:04	36.56	804	12.69	2019 Jul	74	101
NGC 3690	11:28:31.0	+58:33:48	111.42	3159	47.74	2019 Feb	102	82
NGC 3810	11:40:57.8	+11:28:18	35.07	1001	15.36	2019 Jul	63	106
NGC 3893	11:48:37.7	+48:42:45	36.80	892	16.35	2019 Jul	78	105
IC 694	11:28:34.2	+58:33:48	111.42	3100	47.74	2017 Jul	120	83
NGC 3953	11:53:48.4	+52:19:44	31.12	1016	17.58	2019 May	120	115
NGC 4030	12:00:23.8	-01:06:03	50.92	1427	24.50	2019 Jul	81	108
NGC 4041	12:02:12.8	+62:08:07	31.74	1243	22.78	2019 May	100	92
NGC 4088	12:05:35.1	+50:32:24	61.68	696	13.37	2019 Feb	81	98
NGC 4102	12:06:23.6	+52:42:36	70.29	859	16.89	2019 Jul	47	99
NGC 4157	12:11:04.2	+50:29:04	50.67	790	13.30	2019 Jul	71	99
NGC 4217	12:15:50.3	+47:05:30	41.19	1028	17.13	2019 May	102	90
NGC 4254	12:18:51.0	+14:24:50	91.86	2403	15.29	2019 Feb	94	86
NGC 4303	12:21:55.4	+04:28:24	78.74	1570	15.29	2019 Feb	83	92
NGC 4321	12:22:53.9	+15:49:22	68.37	1571	15.20	2019 Jul	48	130
NGC 4414	12:26:26.9	+31:13:24	70.69	720	17.68	2019 Feb	77	85
NGC 4418	12:26:54.7	-00:52:42	31.94	2104	31.90	2019 Feb	81	108
NGC 4501	12:31:57.6	+14:25:20	62.97	2284	15.29	2019 Jul	54	109
NGC 4490	12:30:34.9	+41:38:47	88.61	641	10.48	2019 Feb	102	90
NGC 4535	12:34:19.9	+08:11:52	32.52	1957	15.77	2019 Jul	67	105
NGC 4527	12:34:09.9	+02:39:04	65.68	1771	15.29	2019 Feb	102	85
NGC 4536	12:34:28.5	+02:11:08	44.51	1802	14.92	2019 Feb	138	85
NGC 4568	12:36:33.7	+11:14:32	56.80	2262	15.29	2019 Aug	37	112
NGC 4605	12:40:00.9	+61:36:28	30.55	117	3.90	2019 Jul	64	107
NGC 4631	12:42:07.1	+32:32:33	160.08	630	7.73	2019 Aug	34	94
NGC 4654	12:43:56.6	+13:07:39	37.77	1037	15.29	2019 Aug	47	94
NGC 4736	12:50:52.9	+41:07:15	120.69	323	4.83	2019 Aug	74	86
NGC 4666	12:45:07.7	-00:27:41	85.95	1495	12.82	2019 Jul	41	99
Mrk 231	12:56:14.2	+56:52:25	29.74	12139	175	2017 Jul	153	94
NGC 4826	12:56:42.6	+21:41:05	81.65	349	3.09	2019 Aug	29	82
NGC 5033	13:13:27.2	+36:35:40	50.23	869	13.76	2019 Aug	34	91
NGC 5055	13:15:49.5	+42:01:39	139.82	500	7.96	2019 Aug	40	91
NGC 5054	13:16:59.0	-16:38:04	31.53	1737	23.87	2019 Jul	78	114

Table 1: (continued)

Source Name	RA (J2000)	DEC (J2000)	$F_{100\mu m}$ (Jy)	cz km s^{-1}	Distance (Mpc)	Obs Month (YYYY MM)	t_{int} (minutes)	T_{sys} (K)
NGC 5194	13:29:53.5	+47:11:42	221.21	468	8.63	2019 Aug	81	87
NGC 5195	13:30:00.0	+47:16:00	31.33	450	8.30	2019 Aug	54	90
NGC 5248	13:37:31.8	+08:53:12	53.48	1152	13.82	2019 Jul	84	140
NGC 5247	13:38:03.4	-17:53:04	41.83	1362	18.77	2019 Jul	58	112
NGC 5713	14:40:10.9	-00:17:22	37.28	1904	26.74	2019 Aug	55	119
NGC 5457	14:03:09.0	+54:21:24	252.84	241	6.70	2019 Aug	54	94
NGC 5775	14:53:58.0	+03:32:32	55.64	1642	26.34	2019 Jul	47	94
CGCG 049-057	15:13:12.7	+07:13:30	31.53	3893	59.06	2019 Jul	47	96
NGC 5907	15:15:58.9	+56:18:36	37.43	612	12.08	2019 Aug	102	186
Arp 220	15:34:57.1	+23:30:10	119.25	5450	79.90	2019 Aug	47	94
NGC 6240	16:52:58.6	+02:24:03	26.49	7298	103.86	2017 Jul	38	164
NGC 6822	19:44:56.8	-14:48:24	95.42	-56	0.54	2019 Jul	70	115
NGC 6946	20:34:52.6	+60:09:12	290.69	53	5.32	2017 Jul	51	90

Table 2: Velocity-integrated Intensities

Source Name	$I_{\text{HCN}(1-0)}$ (K km s ⁻¹)	$I_{\text{HCO}^+(1-0)}$ (K km s ⁻¹)	$I_{\text{HNC}(1-0)}$ (K km s ⁻¹)	$I_{\text{CS}(3-2)}$ (K km s ⁻¹)
NGC 891	0.63 ± 0.07	0.65 ± 0.08	0.73 ± 0.13	< 0.29
IC 342	9.40 ± 0.13	7.84 ± 0.11	4.75 ± 0.11	2.45 ± 0.13
UGC 2855	2.82 ± 0.11	2.44 ± 0.12	1.23 ± 0.12	0.59 ± 0.14
NGC 1569	< 0.14	0.34 ± 0.10	< 0.19	< 0.33
NGC 2146	4.15 ± 0.16	5.09 ± 0.27	1.19 ± 0.21	1.22 ± 0.23
NGC 2403	< 0.15	< 0.15	< 0.15	< 0.26
NGC 2683	0.29 ± 0.06	0.12 ± 0.03	< 0.13	< 0.19
NGC 2903	2.69 ± 0.14	2.31 ± 0.14	0.63 ± 0.14	< 0.65
NGC 2976	0.20 ± 0.07	0.10 ± 0.03	< 0.14	0.31 ± 0.09
NGC 3031	< 0.18	0.28 ± 0.05	< 0.12	< 0.37
M 82_1	16 ± 0.04	24 ± 0.07	6.9 ± 0.06	4.94 ± 0.08
M 82_2	26 ± 0.08	39.6 ± 0.09	12.4 ± 0.08	11.35 ± 0.08
M 82_3	27.6 ± 0.07	41.5 ± 0.11	13.4 ± 0.08	12.93 ± 0.45
M 82_4	25.8 ± 0.57	36 ± 0.11	11.4 ± 0.08	9.50 ± 0.33
M 82_5	15 ± 0.06	20 ± 0.10	5.7 ± 0.14	4.31 ± 0.13
NGC 3079	5.6 ± 0.14	5.9 ± 0.56	2.2 ± 0.14	3.12 ± 0.20
NGC 3310	0.38 ± 0.06	0.54 ± 0.09	< 0.13	0.53 ± 0.06
NGC 3351	1.86 ± 0.23	1.47 ± 0.15	0.84 ± 0.11	0.88 ± 0.25
NGC 3368	1.82 ± 0.12	2.29 ± 0.20	0.87 ± 0.16	1.43 ± 0.21
NGC 3504	2.11 ± 0.10	2.04 ± 0.12	0.82 ± 0.14	0.94 ± 0.15
NGC 3521	0.70 ± 0.10	0.30 ± 0.10	< 0.16	< 0.28
NGC 3593	1.01 ± 0.16	1.14 ± 0.11	0.75 ± 0.13	0.58 ± 0.16
NGC 3627	3.26 ± 0.09	2.38 ± 0.07	1.06 ± 0.05	1.34 ± 0.09
NGC 3628	4.32 ± 0.16	4.30 ± 0.17	2.83 ± 0.07	2.09 ± 0.17
NGC 3675	0.68 ± 0.17	0.37 ± 0.12	< 0.29	< 0.40
NGC 3690	1.07 ± 0.08	2.17 ± 0.11	0.80 ± 0.07	0.68 ± 0.09
NGC 3810	0.31 ± 0.10	< 0.18	0.47 ± 0.11	0.69 ± 0.24
NGC 3893	0.76 ± 0.13	0.54 ± 0.11	< 0.22	< 0.36
IC 694	2.66 ± 0.10	4.69 ± 0.11	0.74 ± 0.11	2.01 ± 0.22
NGC 3953	0.31 ± 0.07	0.25 ± 0.05	< 0.11	< 0.15
NGC 4030	2.23 ± 0.11	1.36 ± 0.12	0.91 ± 0.14	0.51 ± 0.13
NGC 4041	2.15 ± 0.07	1.52 ± 0.04	0.85 ± 0.06	0.50 ± 0.07
NGC 4088	0.92 ± 0.05	1.09 ± 0.07	0.25 ± 0.07	< 0.33
NGC 4102	5.16 ± 0.14	3.94 ± 0.16	2.51 ± 0.23	1.42 ± 0.25
NGC 4157	0.54 ± 0.13	0.89 ± 0.27	< 0.19	< 0.33
NGC 4217	0.61 ± 0.07	0.40 ± 0.09	0.33 ± 0.11	< 0.18
NGC 4254	0.60 ± 0.04	0.50 ± 0.06	0.23 ± 0.07	< 0.28
NGC 4303	1.41 ± 0.09	1.20 ± 0.06	0.55 ± 0.07	0.76 ± 0.08
NGC 4321	1.99 ± 0.12	1.28 ± 0.18	1.08 ± 0.20	< 0.53
NGC 4414	2.57 ± 0.21	1.57 ± 0.14	1.04 ± 0.04	< 0.23
NGC 4418	2.48 ± 0.13	1.89 ± 0.11	1.37 ± 0.10	1.91 ± 0.15
NGC 4501	0.92 ± 0.11	0.58 ± 0.15	0.32 ± 0.09	0.48 ± 0.15
NGC 4490	0.28 ± 0.09	0.19 ± 0.04	0.19 ± 0.04	< 0.23
NGC 4535	0.90 ± 0.06	0.41 ± 0.07	0.35 ± 0.08	0.60 ± 0.10
NGC 4527	< 0.10	0.21 ± 0.07	0.21 ± 0.07	< 0.22
NGC 4536	< 0.1	0.23 ± 0.05	< 0.07	< 0.07
NGC 4568	0.99 ± 0.14	0.94 ± 0.20	< 0.37	< 0.59
NGC 4605	< 0.19	< 0.22	< 0.10	< 0.24
NGC 4631	0.64 ± 0.06	1.20 ± 0.08	< 0.24	< 0.31
NGC 4654	< 0.22	< 0.26	< 0.27	< 0.26
NGC 4736	0.91 ± 0.09	0.88 ± 0.11	0.50 ± 0.08	0.52 ± 0.12
NGC 4666	1.41 ± 0.19	1.04 ± 0.14	0.48 ± 0.11	< 0.48
Mrk 231	1.6 ± 0.05	1.2 ± 0.05	0.7 ± 0.03	–
NGC 4826	4.08 ± 0.12	2.91 ± 0.17	1.57 ± 0.19	0.64 ± 0.16
NGC 5033	1.76 ± 0.16	1.76 ± 0.19	0.75 ± 0.31	0.37 ± 0.12
NGC 5055	1.71 ± 0.19	1.37 ± 0.29	0.38 ± 0.13	< 0.34
NGC 5054	0.64 ± 0.12	0.74 ± 0.18	0.29 ± 0.09	0.75 ± 0.14
NGC 5194	4.59 ± 0.14	2.59 ± 0.12	1.27 ± 0.07	< 0.23
NGC 5195	1.40 ± 0.14	2.36 ± 0.14	0.78 ± 0.11	< 0.24
NGC 5248	2.22 ± 0.18	1.17 ± 0.16	0.99 ± 0.15	< 0.30
NGC 5247	0.42 ± 0.09	1.24 ± 0.25	< 0.18	< 0.31
NGC 5713	1.17 ± 0.11	1.05 ± 0.10	0.45 ± 0.09	0.45 ± 0.13
NGC 5457	0.22 ± 0.04	< 0.12	< 0.17	< 0.22

Table 2: (continued)

Source Name	$I_{\text{HCN}(1-0)}$ (K km s ⁻¹)	$I_{\text{HCO}^+(1-0)}$ (K km s ⁻¹)	$I_{\text{HNC}(1-0)}$ (K km s ⁻¹)	$I_{\text{CS}(3-2)}$ (K km s ⁻¹)
NGC 5775	0.60 ± 0.12	0.59 ± 0.08	0.27 ± 0.13	< 0.58
CGCG049-057	2.35 ± 0.21	1.35 ± 0.19	0.88 ± 0.11	1.14 ± 0.20
NGC 5907	0.15 ± 0.05	< 0.12	0.24 ± 0.04	< 0.30
Arp 220	8.58 ± 0.31	3.64 ± 0.30	6.73 ± 0.31	4.97 ± 0.31
NGC 6240	2.7 ± 0.05	2.77 ± 0.40	0.60 ± 0.04	–
NGC 6822	< 0.31	< 0.25	< 0.23	< 0.26
NGC 6946	9.34 ± 0.10	9.05 ± 0.13	3.60 ± 0.30	3.61 ± 0.11

Table 3: Line luminosities and infrared luminosity

Source	$\log L_{\text{HCN}}$ (K km s ⁻¹)	$\log L_{\text{HCO}^+}$ (K km s ⁻¹)	$\log L_{\text{HNC}}$ (K km s ⁻¹)	$\log L_{\text{CS}}$ (K km s ⁻¹)	$\log L_{\text{IR}}^{\text{a}}$ $\log L_{\odot}$	$\log L_{\text{IR}}^{\text{b}}$ $\log L_{\odot}$	Type
NGC 891	5.98 ± 0.05	5.99 ± 0.05	6.04 ± 0.08	< 5.64	9.89 ± 0.11	9.69±0.11	SA(s)b
IC 342	6.61 ± 0.01	6.53 ± 0.01	6.32 ± 0.01	6.02± 0.02	10.14 ± 0.09	10.07±0.09	SAB(rs)cd
*UGC 2855	7.34 ± 0.02	7.28 ± 0.02	6.98 ± 0.04	0.66± 0.10	10.75± 0.09	10.75±0.09	SB
NGC 1569	< 4.79	5.17 ± 0.13	< 5.23	< 5.16	8.86 ± 0.11	8.36±0.11	IBm
NGC 2146	7.36 ± 0.02	7.45 ± 0.02	6.82 ± 0.08	6.83 ± 0.08	10.50 ± 0.11	9.55±0.11	SB
NGC 2403	< 4.51	< 4.51	< 4.28	< 4.74	7.64 ± 0.11	7.04±0.11	SAB(s)cd
NGC 2683	5.51 ± 0.09	5.12 ± 0.11	< 5.16	< 5.32	8.68 ± 0.11	8.24±0.09	SA(rs)b
NGC 2903	6.58 ± 0.02	6.51 ± 0.03	5.95 ± 0.10	< 5.96	9.83 ± 0.09	9.73±0.09	SAB(rs)bc
NGC 2976	4.47 ± 0.15	4.17 ± 0.13	< 4.32	4.66± 0.13	7.59 ± 0.09	7.23±0.11	SAc
NGC 3031	< 4.69	4.88 ± 0.08	< 4.51	< 5.00	8.23 ± 0.11	8.03±0.11	SA(s)ab
M 82_1	6.64 ± 0.001	6.81 ± 0.001	6.27± 0.004	6.13 ± 0.01	10.04 ± 0.11	9.65±0.11	SB
M 82_2	6.85 ± 0.001	7.03 ± 0.001	6.53 ± 0.003	6.49 ± 0.01	10.33±0.11	10.11±0.11	SB
M 82_3	6.87± 0.001	7.05 ± 0.001	6.56±0.003	6.55 ± 0.02	10.31±0.11	9.93±0.11	SB
M 82_4	6.85 ± 0.01	6.99 ± 0.001	6.49±0.003	6.41 ± 0.02	10.27±0.11	10.10±0.11	SB
M 82_5	6.61 ± 0.001	6.73 ± 0.002	6.19 ± 0.01 ± 0.01	6.07 ± 0.01	9.95 ± 0.12	9.50±0.11	SB
NGC 3079	7.58 ± 0.01	7.60 ± 0.04	7.17 ± 0.03	7.32± 0.03	10.77±0.11	10.70±0.11	SB
NGC 3310	6.48 ± 0.07	6.64 ± 0.07	< 6.02	6.63± 0.05	10.54±0.09	10.44±0.11	SB
NGC 3351	6.58 ± 0.05	6.48 ± 0.04	6.23 ± 0.11	6.25± 0.12	9.75±0.11	9.58±0.11	SB(r)b
NGC 3368	6.61 ± 0.03	6.71 ± 0.04	6.29 ± 0.08	6.51± 0.06	9.26±0.09	9.15±0.09	SAB(rs)ab
NGC 3504	7.50 ± 0.02	7.48 ± 0.03	7.09 ± 0.07	7.15 ± 0.07	10.53±0.11	10.44±0.11	SB
NGC 3521	5.83 ± 0.06	5.46 ± 0.14	< 5.19	< 5.43	9.18±0.11	8.70±0.11	SAB(rs)bc
NGC 3593	5.72 ± 0.26	5.77 ± 0.04	5.59 ± 0.08	5.48±0.12	9.17±0.09	9.03±0.09	SA(s)
NGC 3627	6.83 ± 0.01	6.69 ± 0.01	6.34 ± 0.02	6.44±0.03	9.73±0.11	9.54±0.11	SB
NGC 3628	6.95 ± 0.02	6.95 ± 0.02	6.77 ± 0.01	6.64±0.04	10.28±0.11	10.13±0.11	SB
NGC 3675	6.35 ± 0.11	6.09 ± 0.14	< 5.98	< 6.12	9.50 ± 0.09	9.26±0.09	SA(s)b
NGC 3690	7.69 ± 0.03	8.00 ± 0.02	7.56 ± 0.04	7.49 ± 0.06	11.57±0.12	10.13 ± 0.11	SB
*NGC 3810	6.17 ± 0.14	< 5.94	6.36 ± 0.10	6.52±0.15	10.12±0.09	10.12±0.11	SB
*NGC 3893	6.62 ± 0.07	6.47 ± 0.09	< 6.08	< 6.30	10.20±0.09	10.20±0.09	SB
IC 694	8.08 ± 0.02	8.33 ± 0.01	7.52 ± 0.06	7.96±0.05	11.74±0.11	11.65±0.11	SB
NGC 3953	6.29±0.10	6.20±0.09	< 5.84	< 5.98	8.96 ± 0.09	8.77±0.11	SB(r)bc
NGC 4030	7.43 ± 0.02	7.22 ± 0.04	7.05 ± 0.07	6.79±0.11	10.35±0.11	10.03±0.09	SB
NGC 4041	7.36 ± 0.01	7.21 ± 0.01	6.95 ± 0.03	6.72±0.06	10.35±0.11	10.19±0.09	SB
NGC 4088	6.53 ± 0.02	6.60 ± 0.03	5.96 ± 0.12	< 6.08	9.76±0.11	9.48±0.09	SB
NGC 4102	7.48 ± 0.01	7.36 ± 0.02	7.17 ± 0.04	6.92±0.08	10.46±0.11	10.35±0.11	SB/AGN
NGC 4157	6.29 ± 0.10	6.51 ± 0.13	5.84 ± 0.00	< 6.08	9.66±0.09	9.42 ± 0.09	SB
NGC 4217	6.56 ± 0.05	6.38 ± 0.10	6.30 ± 0.14	< 6.03	9.83±0.11	9.56±0.11	SB
NGC 4254	6.45 ± 0.03	6.37 ± 0.05	6.03 ± 0.13	< 6.12	9.78±0.11	9.56 ± 0.11	SB
NGC 4303	6.83 ± 0.03	6.76 ± 0.02	6.42 ± 0.06	6.56±0.05	9.60±0.11	9.46±0.11	SB
NGC 4321	6.97 ± 0.03	6.78 ± 0.06	6.71 ± 0.08	< 6.40	9.73±0.11	9.53±0.09	SB
NGC 4414	7.22 ± 0.04	7.00 ± 0.04	6.82 ± 0.02	< 6.17	10.26±0.09	9.88±0.09	SB
NGC 4418	7.71 ± 0.02	7.59 ± 0.03	7.45 ± 0.03	7.60±0.03	10.99±0.09	10.98±0.11	SB/AGN
NGC 4501	6.64 ± 0.05	6.44 ± 0.11	6.18 ± 0.12	6.35±0.14	9.56±0.09	9.23±0.11	SB/AGN
NGC 4490	5.75 ± 0.14	5.58 ± 0.09	5.58 ± 0.09	< 5.71	9.70±0.09	9.41±0.09	SB
NGC 4535	6.66 ± 0.03	6.31 ± 0.07	6.25 ± 0.10	6.48±0.07	9.43±0.11	9.23±0.09	SB
NGC 4527	< 5.68	6.00 ± 0.14	6.00 ± 0.14	< 6.02	9.55±0.11	8.68±0.11	SB
NGC 4536	< 5.65	6.02 ± 0.09	< 5.56	< 5.50	9.67±0.11	9.86±0.11	SB
NGC 4568	6.67 ± 0.06	6.65 ± 0.09	< 6.25	< 6.44	9.28±0.11	8.77±0.11	SB
NGC 4605	4.78 ± 0.00	4.84 ± 0.00	< 4.50	< 4.88	8.35±0.09	7.95±0.09	SB(s)c
NGC 4631	5.89 ± 0.04	6.17 ± 0.03	< 5.47	< 5.58	9.54±0.11	9.23±0.11	SB
NGC 4654	< 6.02	< 6.09	< 6.11	< 6.09	9.59±0.11	9.30±0.11	SB
NGC 4736	5.64 ± 0.04	5.63 ± 0.05	5.38 ± 0.07	5.40 ± 0.10	9.20±0.11	8.96±0.11	AGN
NGC 4666	6.67 ± 0.06	6.54 ± 0.06	6.21 ± 0.10	< 6.21	9.74±0.11	9.15±0.11	SB
Mrk 231	8.94 ± 0.01	8.81 ± 0.03	8.58 ± 0.02	–	12.39±0.11	8.96±0.11	SB
NGC 4826	5.90 ± 0.01	5.76 ± 0.03	5.49 ± 0.05	5.10 ± 0.12	8.80±0.11	8.42±0.11	AGN
NGC 5033	6.83 ± 0.04	6.83 ± 0.05	6.46 ± 0.18	6.17±0.14	9.29±0.11	9.01±0.11	SB/AGN
NGC 5055	6.35 ± 0.05	6.25 ± 0.09	5.69 ± 0.15	< 5.65	9.42±0.11	9.01±0.11	SB
*NGC 5054	6.87 ± 0.08	6.93 ± 0.11	6.53 ± 0.13	6.94±0.08	10.34±0.09	10.34±0.09	SB
NGC 5194	6.85 ± 0.01	6.60 ± 0.02	6.29 ± 0.02	< 5.55	9.53±0.11	9.07±0.11	SB/AGN
NGC 5195	6.30 ± 0.04	6.52 ± 0.03	6.04 ± 0.06	< 5.53	9.30±0.12	9.21±0.11	I0
NGC 5248	6.94 ± 0.04	6.66 ± 0.06	6.59 ± 0.07	< 6.07	9.79±0.11	9.54 ± 0.11	SB
NGC 5247	6.48 ± 0.09	6.95 ± 0.09	6.11 ± 0.00	< 6.35	9.68±0.09	9.50±0.09	SB
NGC 5713	7.23 ± 0.04	7.18 ± 0.08	6.81 ± 0.87	6.81±0.13	10.54±0.11	10.33±0.11	SB
NGC 5457	5.31 ± 0.08	< 5.04	< 5.20	< 5.31	7.96±0.14	7.40 ± 0.11	SB

Table 3: (continued)

Source	$\log L_{\text{HCN}}$ (K km s ⁻¹)	$\log L_{\text{HCO}^+}$ (K km s ⁻¹)	$\log L_{\text{HNC}}$ (K km s ⁻¹)	$\log L_{\text{CS}}$ (K km s ⁻¹)	$\log L_{\text{IR}}$ ($\log L_{\odot}$)	$\log L_{\text{IR}}$ ($\log L_{\odot}$)	Type
NGC 5775	6.93 ± 0.09	6.92 ± 0.07	< 6.60	< 6.91	10.32±0.09	10.10±0.09	SB
CGCG049-057	8.21 ± 0.04	7.97 ± 0.06	7.78 ± 0.05	7.90±0.08	11.34±0.11	11.20±0.11	SB
NGC 5907	5.65 ± 0.14	< 5.56	5.86 ± 0.07	< 5.95	9.06±0.11	8.63±0.11	SA(s)c
Arp 220	9.03 ± 0.02	8.66 ± 0.04	8.92 ± 0.02	8.67 ± 0.04	12.19±0.11	12.16±0.11	SB/AGN
NGC 6240	8.75 ± 0.01	8.76 ± 0.06	8.09 ± 0.03	–	11.83±0.11	11.78±0.11	SB/AGN
NGC 6822	< 3.27	< 3.18	< 3.14	< 3.19	5.28±0.15	4.78±0.11	IB(s)m
NGC 6946	6.74 ± 0.00	6.72 ± 0.01	6.32 ± 0.04	5.98±0.03	9.63±0.11	9.53±0.11	SB
IRAS17208	9.11 ± 0.03	9.00 ± 0.04	9.00 ± 0.05	–	12.46±0.11	–	SB
IC 860	7.96 ± 0.05	7.76 ± 0.06	7.69 ± 0.07	–	11.19±0.11	–	SB
NGC 1614	7.86 ± 0.16	8.13 ± 0.09	7.33 ± 0.42	–	11.51±0.11	–	SB
NGC 4388	6.46 ± 0.08	6.61 ± 0.06	6.09 ± 0.18	–	9.52 ± 0.11	–	SB/AGN
NGC 6090	8.20 ± 0.07	8.43 ± 0.04	7.60 ± 0.22	–	11.40±0.12	–	SB
NGC 7469	8.29 ± 0.02	8.34 ± 0.02	8.03 ± 0.04	–	11.51±0.11	–	SB/AGN
NGC 7771	8.41 ± 0.02	8.37 ± 0.02	8.18 ± 0.04	–	11.29±0.11	–	SB
NGC 660	7.24 ± 0.02	7.26 ± 0.02	6.96 ± 0.03	–	9.86±0.09	–	SB/AGN
NGC 3556	6.39 ± 0.06	6.59 ± 0.04	5.87 ± 0.21	–	9.31±0.09	–	SB
NGC 1068	7.99 ± 0.01	7.82 ± 0.01	7.60 ± 0.02	–	10.77±0.11	–	SB/AGN
*UGC 2866	7.15 ± 0.04	7.32 ± 0.02	6.86 ± 0.07	–	10.68±0.09	–	SB
NGC 2273	7.02 ± 0.08	6.80 ± 0.13	6.80 ± 0.13	–	10.18±0.11	–	SB/AGN
NGC 34	7.92 ± 0.07	8.13 ± 0.06	< 7.71	–	11.44±0.09	–	SB/AGN
MCG –02-01-052	8.08 ± 0.10	< 7.76	< 7.74	–	11.41±0.09	–	SB
MCG –02-01-051	7.56 ± 0.13	7.81 ± 0.10	< 7.53	–	11.41±0.09	–	SB
IC 1623	8.26 ± 0.04	8.68 ± 0.02	7.88 ± 0.09	–	11.65±0.09	–	SB
MCG –03-04-014	8.51 ± 0.06	8.51 ± 0.04	8.12 ± 0.14	–	11.63±0.09	–	SB
IRAS 01364-1042	< 8.65	< 8.46	< 8.54	–	11.76±0.09	–	SB/AGN
IC 214	7.97 ± 0.12	8.16 ± 0.09	< 7.56	–	11.37±0.09	–	SB
NGC 0958	< 7.91	< 7.82	< 7.89	–	11.17±0.09	–	SB
ESO 550-IG 025	8.13 ± 0.11	8.03 ± 0.13	< 8.07	–	11.45±0.09	–	SB
UGC 3094	< 7.88	8.13 ± 0.08	< 7.87	–	11.35±0.09	–	SB
NGC 1797	7.70 ± 0.10	7.58 ± 0.09	< 7.47	–	11.00±0.09	–	SB
VII Zw 31	< 8.90	9.01 ± 0.14	< 8.89	–	11.94±0.09	–	SB
IRAS F05189-2524	8.58 ± 0.08	8.45 ± 0.10	8.30 ± 0.12	–	12.11±0.09	–	SB/AGN
IRAS F05187-1017	8.25 ± 0.06	8.26 ± 0.08	< 7.63	–	11.23±0.09	–	SB
IRAS F06076-2139	8.63 ± 0.08	< 8.38	< 8.31	–	11.59±0.09	–	SB
NGC 2341	7.57 ± 0.00	< 7.66	< 7.81	–	11.25±0.09	–	SB
NGC 2342	7.84 ± 0.07	7.88 ± 0.08	< 7.35	–	11.25±0.09	–	SB
IRAS 07251+0248	8.82 ± 0.14	< 8.80	< 8.88	–	12.32±0.09	–	SB
NGC 2623	8.49 ± 0.08	8.45 ± 0.10	< 8.16	–	11.54±0.09	–	SB
IRAS 09111-1007W	8.70 ± 0.06	8.84 ± 0.08	< 8.32	–	12.00±0.09	–	SB/AGN
IRAS 09111-1007E	< 8.55	< 8.61	< 8.54	–	12.00±0.09	–	SB
UGC 5101	9.00 ± 0.04	8.76 ± 0.06	8.63 ± 0.09	–	11.95±0.09	–	SB/AGN
CGCG 011-076	8.37 ± 0.06	8.41 ± 0.06	< 7.88	–	11.37±0.09	–	SB
IRAS F12224-0624	< 8.13	< 8.21	< 8.21	–	11.27±0.09	–	SB
CGCG 043-099	< 8.39	< 8.38	< 8.38	–	11.62±0.09	–	SB
ESO 507-G 070	8.34 ± 0.07	8.52 ± 0.05	7.94 ± 0.12	–	11.49±0.09	–	SB/AGN
NGC 5104	8.21 ± 0.08	7.99 ± 0.12	< 7.74	–	11.2 ± 0.09	–	SB
IC 4280	8.02 ± 0.10	8.11 ± 0.09	7.80 ± 0.14	–	11.08±0.09	–	SB
NGC 5257	7.86 ± 0.11	7.94 ± 0.08	7.84 ± 0.13	–	11.55±0.09	–	SB
NGC 5258	7.91 ± 0.10	8.00 ± 0.06	7.75 ± 0.12	–	11.55±0.09	–	SB
UGC 8739	8.15 ± 0.06	8.01 ± 0.09	7.98 ± 0.09	–	11.08±0.09	–	SB
NGC 5331	8.39 ± 0.06	8.21 ± 0.10	< 8.19	–	11.59±0.09	–	SB
CGCG 247-020	8.33 ± 0.07	8.10 ± 0.09	7.89 ± 0.11	–	11.32±0.09	–	SB
IRAS F14348-1447	8.97 ± 0.00	< 8.82	< 8.96	–	12.30±0.09	–	SB
CGCG 049-057	8.35 ± 0.04	8.01 ± 0.06	8.07 ± 0.07	–	11.27±0.09	–	SB
NGC 5936	7.95 ± 0.06	7.77 ± 0.06	< 7.53	–	11.07±0.09	–	SB
ARP 220	9.18 ± 0.03	8.88 ± 0.05	8.99 ± 0.03	–	12.21±0.09	–	SB/AGN
IRAS F16164-0746	8.14 ± 0.09	8.38 ± 0.06	7.92 ± 0.12	–	11.55±0.09	–	SB
CGCG 052-037	8.15 ± 0.08	8.19 ± 0.06	8.19 ± 0.08	–	11.38±0.09	–	SB
IRAS F16399-093	8.28 ± 0.06	8.23 ± 0.06	7.98 ± 0.13	–	11.56±0.09	–	SB
NGC 6285	< 7.65	< 7.49	< 7.64	–	11.56±0.09	–	SB
NGC 6286	8.31 ± 0.06	8.32 ± 0.05	< 7.70	–	11.32±0.09	–	SB
IRAS F17138-1017	7.97 ± 0.05	8.06 ± 0.05	7.72 ± 0.10	–	11.42±0.09	–	SB
UGC 11041	8.16 ± 0.07	8.16 ± 0.06	< 7.75	–	11.04 ± 0.09	–	SB
CGCG 141-034	8.15 ± 0.09	< 7.83	< 7.98	–	11.13±0.09	–	SB

Table 3: (continued)

Source	$\log L_{\text{HCN}}$ (K km s ⁻¹)	$\log L_{\text{HCO}^+}$ (K km s ⁻¹)	$\log L_{\text{HNC}}$ (K km s ⁻¹)	$\log L_{\text{CS}}$ (K km s ⁻¹)	$\log L_{\text{IR}}$ (log L _⊙)	$\log L_{\text{IR}}$ (log L _⊙)	Type
IRAS 18090+0130	8.26 ± 0.06	8.33 ± 0.06	7.88 ± 0.12	–	11.58±0.09	–	SB
NGC 6701	8.25 ± 0.03	8.16 ± 0.04	7.87 ± 0.08	–	11.05±0.09	–	SB
NGC 6786	8.01 ± 0.07	8.05 ± 0.09	7.85 ± 0.11	–	11.43±0.09	–	SB/AGN
UGC 11415	7.75 ± 0.00	8.04 ± 0.10	< 7.65	–	11.43±0.09	–	SB
ESO 593-IG 008	< 8.83	< 8.92	< 8.86	–	11.87±0.09	–	SB
NGC 6907	7.97 ± 0.06	7.71 ± 0.09	7.42 ± 0.07	–	11.03±0.09	–	SB
IRAS 21101+5810	8.37 ± 0.07	8.17 ± 0.11	7.99 ± 0.01	–	11.75±0.09	–	SB
ESO 602-G 025	8.20 ± 0.11	8.16 ± 0.07	8.15 ± 0.12	–	11.27±0.09	–	SB/AGN
UGC 12150	8.28 ± 0.05	8.35 ± 0.04	7.86 ± 0.12	–	11.29±0.09	–	SB
IRAS F22491-1808	< 9.09	< 9.04	< 9.03	–	12.11±0.09	–	SB
CGCG 453-062	8.26 ± 0.07	7.95 ± 0.14	< 7.90	–	11.31±0.09	–	SB
NGC 7591	8.06 ± 0.06	7.76 ± 0.08	7.76 ± 0.13	–	11.05±0.09	–	SB/AGN
IRAS F23365+3604	8.94 ± 0.14	9.14 ± 0.09	< 8.98	–	12.13±0.09	–	SB/AGN

Notes. ^a The measured the IR emission within the beam-size of 28". ^b The measured the IR emission within the beam-size of 17". For the sources in [Privon et al. \(2015\)](#), the infrared luminosity is from [Sanders et al. \(2003\)](#) and the uncertainties of L_{IR} are assumed to be 20%.

REFERENCES

- Aalto S., Polatidis A. G., Hüttemeister S., Curran S. J., 2002, *A&A*, 381, 783. doi:10.1051/0004-6361:20011514
- Balog Z., Müller T., Nielbock M., Altieri B., Klaas U., Blommaert J., Linz H., et al., 2014, *ExA*, 37, 129. doi:10.1007/s10686-013-9352-3
- Bussmann R. S., Narayanan D., Shirley Y. L., Juneau S., Wu J., Solomon P. M., Vanden Bout P. A., et al., 2008, *ApJL*, 681, L73. doi:10.1086/590181
- Cao Y., Wong T., Xue R., Bolatto A. D., Blitz L., Vogel S. N., Leroy A. K., et al., 2017, *ApJ*, 847, 33. doi:10.3847/1538-4357/aa88c5
- Costagliola F., Sakamoto K., Muller S., Martín S., Aalto S., Harada N., van der Werf P., et al., 2015, *A&A*, 582, A91. doi:10.1051/0004-6361/201526256
- Costagliola F., Aalto S., Rodriguez M. I., Muller S., Spoon H. W. W., Martín S., Pérez-Torres M. A., et al., 2011, *A&A*, 528, A30. doi:10.1051/0004-6361/201015628
- Foreman-Mackey D., Hogg D. W., Lang D., Goodman J., 2013, *PASP*, 125, 306. doi:10.1086/670067
- Galametz M., Kennicutt R. C., Calzetti D., Aniano G., Draine B. T., Boquien M., Brandl B., et al., 2013, *MNRAS*, 431, 1956. doi:10.1093/mnras/stt313
- Gao Y., Solomon P. M., 2004, *ApJ*, 606, 271. doi:10.1086/382999
- Gao Y., Carilli C. L., Solomon P. M., Vanden Bout P. A., 2007, *ApJL*, 660, L93. doi:10.1086/518244
- García-Burillo S., Usero A., Alonso-Herrero A., Graciá-Carpio J., Pereira-Santaella M., Colina L., Planesas P., et al., 2012, *A&A*, 539, A8. doi:10.1051/0004-6361/201117838
- Graciá-Carpio J., García-Burillo S., Planesas P., Colina L., 2006, *ApJL*, 640, L135. doi:10.1086/503361
- Graciá-Carpio J., García-Burillo S., Planesas P., Fuente A., Usero A., 2008, *A&A*, 479, 703. doi:10.1051/0004-6361:20078223
- Greve T. R., Papadopoulos P. P., Gao Y., Radford S. J. E., 2009, *ApJ*, 692, 1432. doi:10.1088/0004-637X/692/2/1432
- Imanishi M., Nakanishi K., Kuno N., Kohno K., 2004, *AJ*, 128, 2037. doi:10.1086/424620
- Imanishi M., Nakanishi K., Tamura Y., Oi N., Kohno K., 2007, *AJ*, 134, 2366. doi:10.1086/523598
- Israel F. P., Tacconi L. J., Baas F., 1995, *A&A*, 295, 599
- Izumi T., Kohno K., Aalto S., Espada D., Fathi K., Harada N., Hatsukade B., et al., 2016, *ApJ*, 818, 42. doi:10.3847/0004-637X/818/1/42
- Izumi T., Kohno K., Martín S., Espada D., Harada N., Matsushita S., Hsieh P.-Y., et al., 2013, *PASJ*, 65, 100. doi:10.1093/pasj/65.5.100
- Kennicutt R. C., 1998, *ApJ*, 498, 541. doi:10.1086/305588
- Kohno K., Matsushita S., Vila-Vilaró B., Okumura S. K., Shibatsuka T., Okiura M., Ishizuki S., et al., 2001, *ASPC*, 249, 672
- Krips M., Neri R., García-Burillo S., Martín S., Combes F., Graciá-Carpio J., Eckart A., 2008, *ApJ*, 677, 262. doi:10.1086/527367
- Lada C. J., Forbrich J., Lombardi M., Alves J. F., 2012, *ApJ*, 745, 190. doi:10.1088/0004-637X/745/2/190
- Li F., Wang J., Kong M., Li S., 2019, *MNRAS*, 482, 4763. doi:10.1093/mnras/sty2880
- Li F., Wang J., Fang M., Li S., Zhang Z.-Y., Gao Y., Kong M., 2020, *MNRAS*, 494, 1095. doi:10.1093/mnras/staa676
- Li F., Wang J., Fang M., Tan Q.-H., Zhang Z.-Y., Gao Y., Li S., 2020, *PASJ*, 72, 41. doi:10.1093/pasj/psaa025
- Lindberg J. E., Aalto S., Muller S., Martí-Vidal I., Falstad N., Costagliola F., Henkel C., et al., 2016, *A&A*, 587, A15. doi:10.1051/0004-6361/201527457
- Mao R.-Q., Schulz A., Henkel C., Mauersberger R., Muders D., Dinh-V-Trung, 2010, *ApJ*, 724, 1336. doi:10.1088/0004-637X/724/2/1336
- Privon G. C., Herrero-Illana R., Evans A. S., Iwasawa K., Perez-Torres M. A., Armus L., Díaz-Santos T., et al., 2015, *ApJ*, 814, 39. doi:10.1088/0004-637X/814/1/39
- Privon G. C., Ricci C., Aalto S., Viti S., Armus L., Díaz-Santos T., González-Alfonso E., et al., 2020, *ApJ*, 893, 149. doi:10.3847/1538-4357/ab8015
- Sanders D. B., Mazzarella J. M., Kim D.-C., Surace J. A., Soifer B. T., 2003, *AJ*, 126, 1607. doi:10.1086/376841
- Schmidt M., 1959, *ApJ*, 129, 243. doi:10.1086/146614
- Shirley Y. L., 2015, *PASP*, 127, 299. doi:10.1086/680342
- Solomon P. M., Downes D., Radford S. J. E., 1992, *ApJL*, 387, L55. doi:10.1086/186304
- Tan Q.-H., Gao Y., Zhang Z.-Y., Greve T. R., Jiang X.-J., Wilson C. D., Yang C.-T., et al., 2018, *ApJ*, 860, 165. doi:10.3847/1538-4357/aac512
- Vila-Vilaro B., Cepa J., Zabludoff A., 2015, *ApJS*, 218, 28. doi:10.1088/0067-0049/218/2/28
- Wang J., Zhang Z., Shi Y., 2011, *MNRAS*, 416, L21. doi:10.1111/j.1745-3933.2011.01090.x
- Wang J., Zhang Z.-Y., Qiu J., Shi Y., Zhang J., Fang M., 2014, *ApJ*, 796, 57. doi:10.1088/0004-637X/796/1/57
- Wang J., Zhang Z.-Y., Zhang J., Shi Y., Fang M., 2016, *MNRAS*, 455, 3986. doi:10.1093/mnras/stv2580
- Wu J., Evans N. J., Gao Y., Solomon P. M., Shirley Y. L., Vanden Bout P. A., 2005, *ApJL*, 635, L173. doi:10.1086/499623
- Zhang Z.-Y., Gao Y., Henkel C., Zhao Y., Wang J., Menten K. M., Güsten R., 2014, *ApJL*, 784, L31. doi:10.1088/2041-8205/784/2/L31

**APPENDIX A: SPECTRA OF DENSE GAS TRACERS FOR
INDIVIDUAL GALAXIES**

This paper has been typeset from a $\text{\TeX}/\text{\LaTeX}$ file prepared by the author.

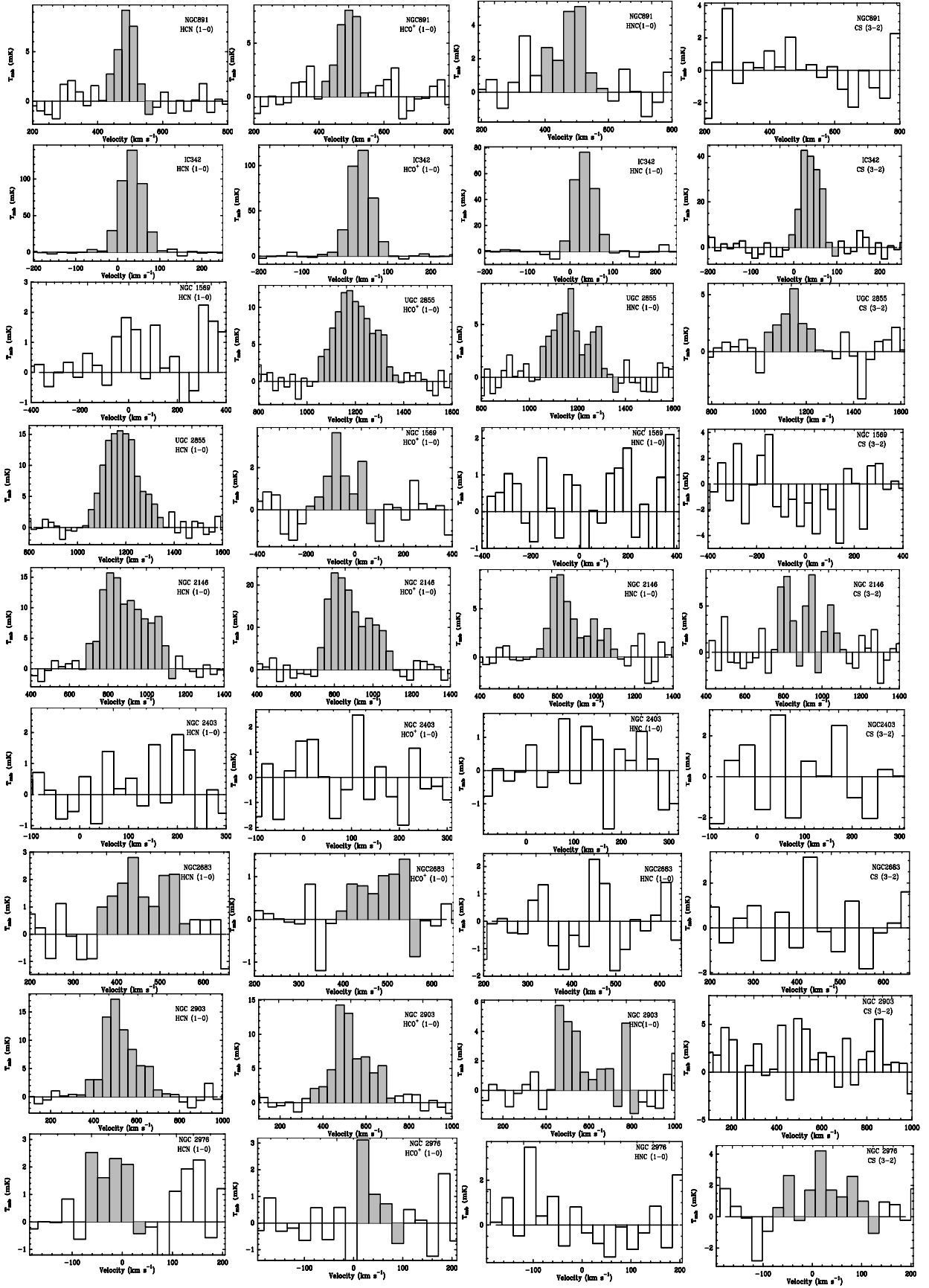


Figure A1. The grey-filled black spectra shown in each subfigure are the detected lines, otherwise, the spectra just shown the marginal detection or the non-detection of those molecular transitions.

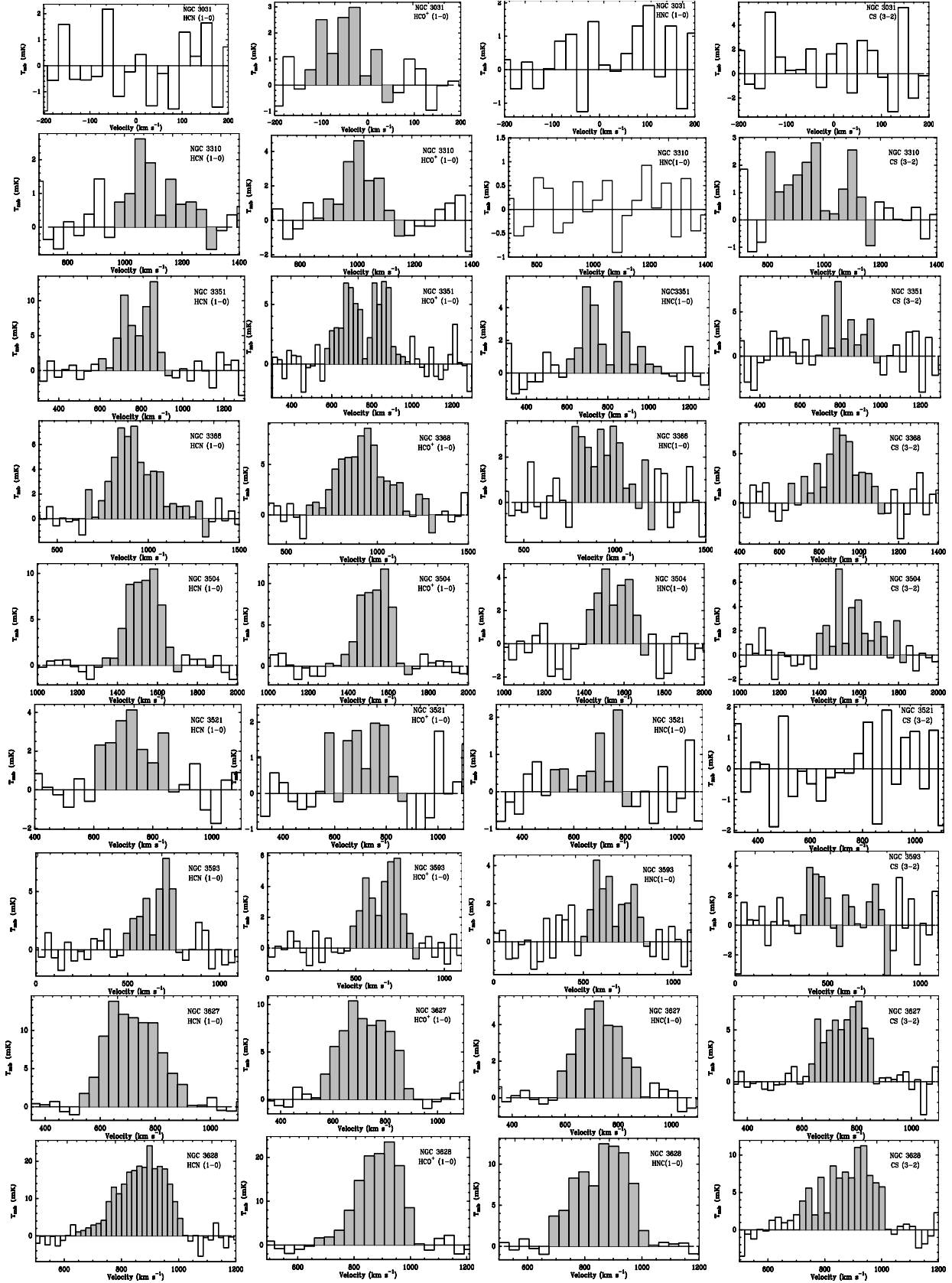


Figure A1 – continued

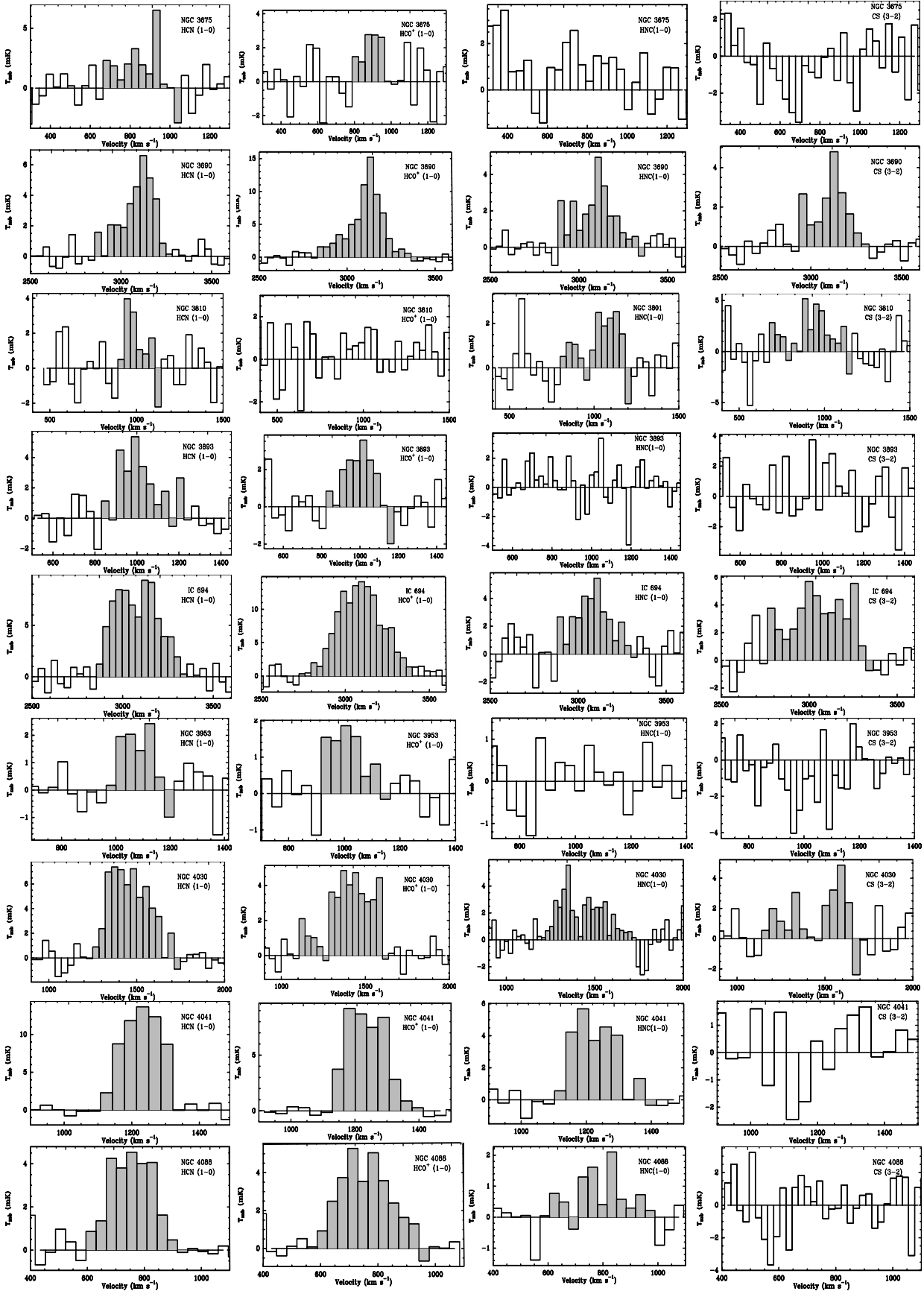


Figure A1 – continued

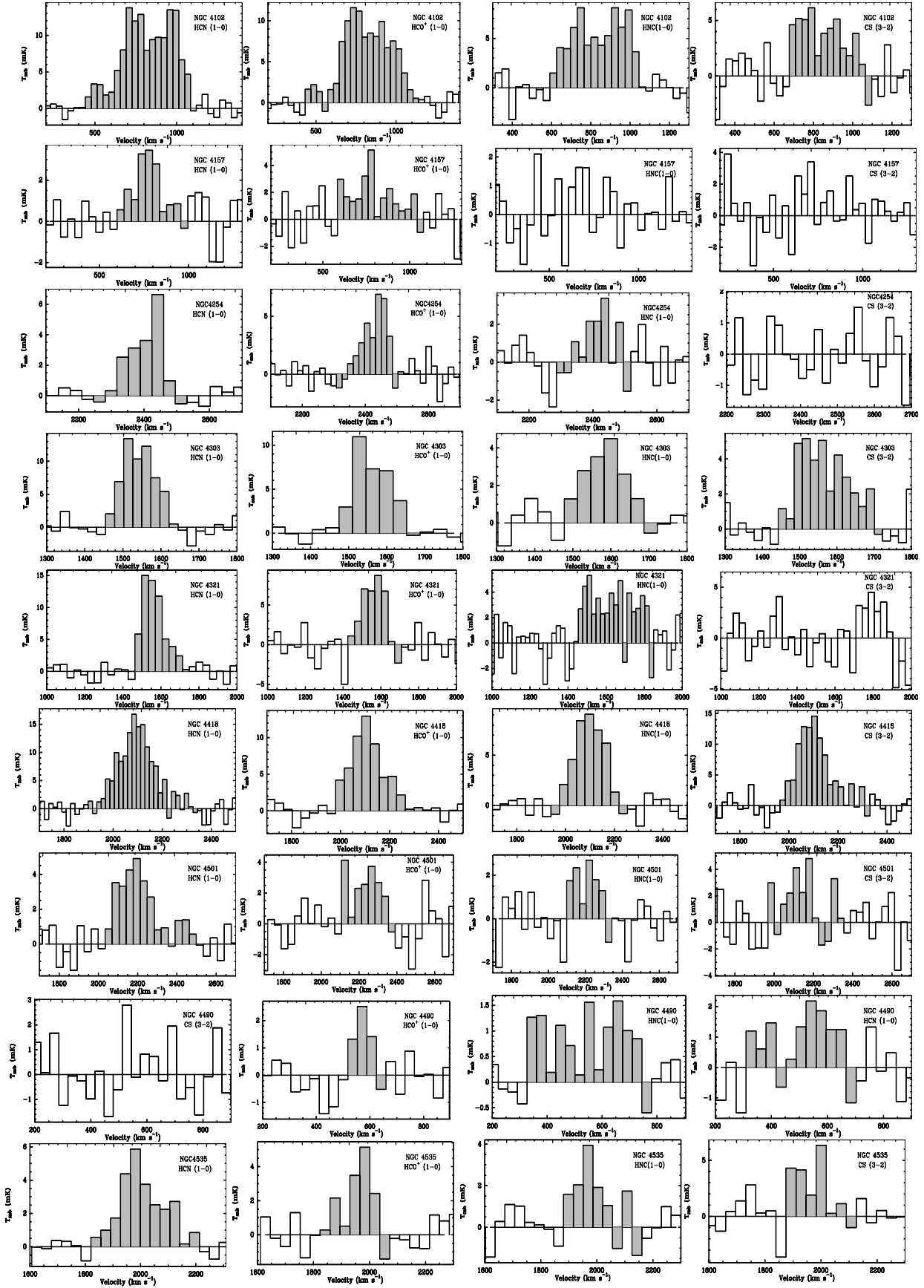


Figure A1 – *continued*

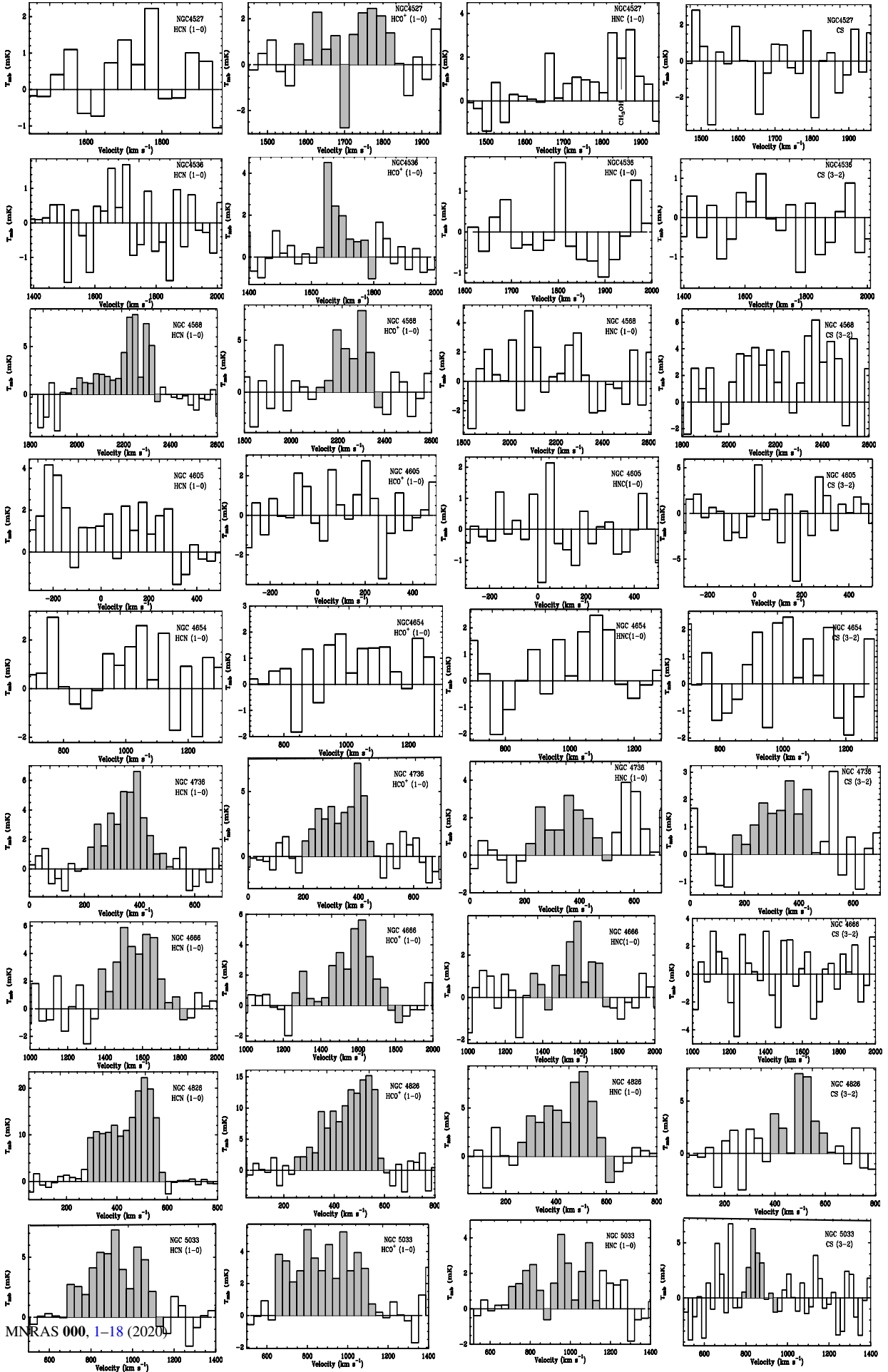


Figure A1 – continued

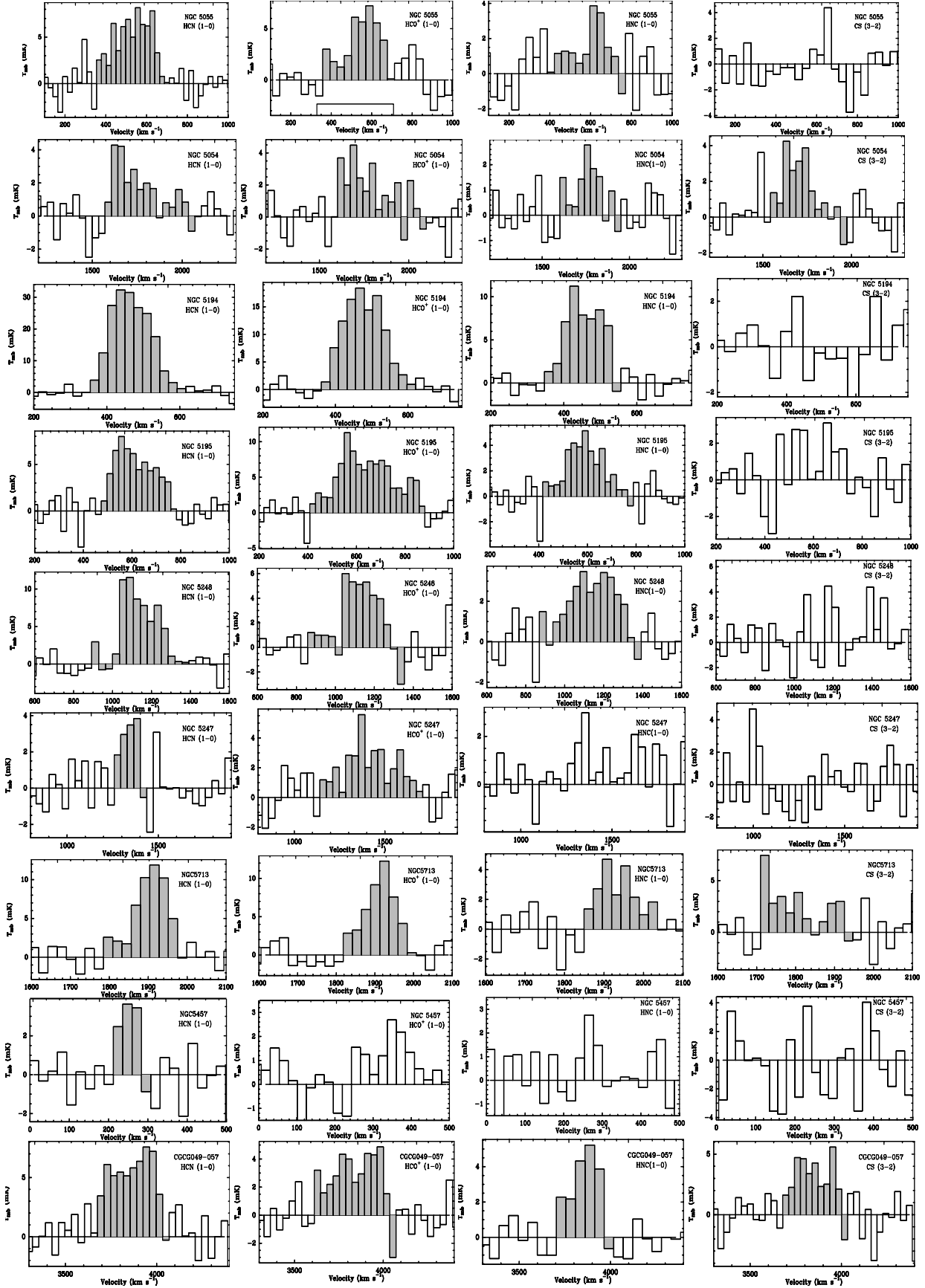


Figure A1 – continued

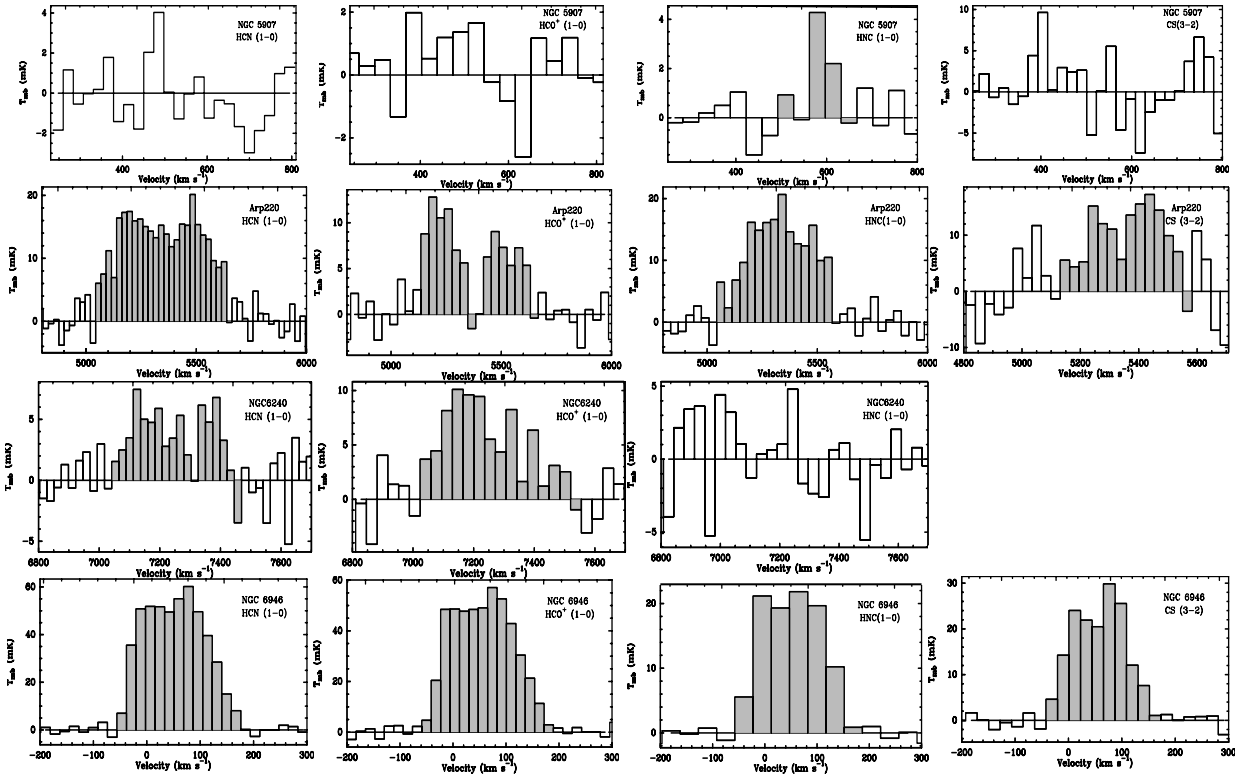


Figure A1 – continued